geosciences

MDPI

Review

Geophysical Survey and Monitoring of Transportation Infrastructure Slopes (TISs): A Review

Zeynab Rosa Maleki [1,2,*], Paul Wilkinson [2], Jonathan Chambers [2], Shane Donohue [3], Jessica Lauren Holmes [1] and Ross Stirling [1]

[1] Faculty of Science, Agriculture & Engineering, School of Engineering, Newcastle University, Newcastle upon Tyne NE1 7RU, UK; jessica.holmes@newcastle.ac.uk (J.L.H.); ross.stirling@newcastle.ac.uk (R.S.)
[2] British Geological Survey, Nicker Hill, Keyworth, Nottingham NG12 5GG, UK; pbw@bgs.ac.uk (P.W.); jecha@bgs.ac.uk (J.C.)
[3] School of Civil Engineering, UCD College of Engineering & Architecture, University College Dublin, Belfield, Dublin 4, D04 V1W8 Dublin, Ireland; shane.donohue@ucd.ie
* Correspondence: z.maleki2@newcastle.ac.uk or zm1@bgs.ac.uk

Abstract: This review examines the application of the geophysical methods for Transportation Infrastructure Slope Monitoring (TISM). In contrast to existing works, which address geophysical methods for natural landslide monitoring, this study focuses on their application to infrastructure assets. It addresses the key aspects regarding the geophysical methods most employed, the subsurface properties revealed, and the design of monitoring systems, including sensor deployment. It evaluates the benefits and challenges associated with each geophysical approach, explores the potential for integrating geophysical techniques with other methods, and identifies the emerging technologies. Geophysical techniques such as Electrical Resistivity Tomography (ERT), Multichannel Analysis of Surface Waves (MASW), and Fiber Optic Cable (FOC) have proven effective in monitoring slope stability and detecting subsurface features, including soil moisture dynamics, slip surfaces, and material heterogeneity. Both temporary and permanent monitoring setups have been used, with increasing interest in real-time monitoring solutions. The integration of advanced technologies like Distributed Acoustic Sensing (DAS), UAV-mounted sensors, and artificial intelligence (AI) promises to enhance the resolution, accessibility, and predictive capabilities of slope monitoring systems. The review concludes with recommendations for future research, emphasizing the need for integrated monitoring frameworks that combine geophysical data with real-time analysis to improve the safety and efficiency of transportation infrastructure management.

Keywords: Geophysical techniques; slope stability; transportation infrastructure slope; monitoring

Academic Editor: Piotr Migoń

Received: 28 February 2025
Revised: 29 April 2025
Accepted: 4 May 2025
Published: 12 June 2025

Citation: Maleki, Z.R.; Wilkinson, P.; Chambers, J.; Donohue, S.; Holmes, J.L.; Stirling, R. Geophysical Survey and Monitoring of Transportation Infrastructure Slopes (TISs): A Review. *Geosciences* **2025**, *15*, 220. https://doi.org/10.3390/geosciences15060220

1. Introduction

Engineered slopes in railway, road, and canal networks have always been essential components of transportation infrastructure and crucial for the development of societies and economies [1]. These slopes deteriorate over time, and failures can happen as a result of a variety of drivers including heavy rain, seasonal drying and wetting cycles, seismic activity, or human activities such as mining or construction. Furthermore, landslides on natural slopes adjacent to transportation infrastructure are subject to similar pressures and risks [2]. Transportation Infrastructure Slopes (TISs) are defined here as either natural or engineered slopes located adjacent to railways, roads, or canal networks.

The socioeconomic impact of TIS instability continues to grow driven by increasing environmental pressures coupled with the strain of a growing population [3]. With 22,000 passenger trains carrying 4.4 million passengers daily and 11% of the nation's daily freight traffic, rail transport is of enormous socioeconomic importance to the UK (e.g., ref. [4]). Any disruption to even a small portion of this network could have disproportionately large knock-on effects across the network. For instance, even a small-scale earthwork failure near to Birmingham caused by the storms that hit the UK on 28 June 2012 resulted in numerous cancellations and delays that reached as far as Penzance, South Wales, Liverpool, Southampton, London, and Edinburgh, totalling 4900 delay minutes [5]. Likewise, at the same time (28 June 2012), a rainfall-induced slope failure that derailed a train in the Scottish Highlands resulted in an 11-day line closure and 10,000 weather-related minutes of delay [5]. More recently Network Rail highlighted several earthwork failures following a persistently wet winter, exacerbated by multiple storms including storm Ciara in February 2020, with failures especially common in the Southern Region. The failure caused major disruptions on the railway between London, the West Midlands, Northwest, and Cumbria [6,7]. However, ref. [8] announced that over successive 5-year control periods of TISM, the frequency of derailments and high-consequence failures has generally decreased although the occurrence of low-frequency, high-consequence events has remained above NR's corporate risk tolerance. Besides the abovementioned UK TIS failures, other regions of the world have been facing even greater challenges. For example, ref. [3] refer to the Andes Mountain region of Ecuador and the Pan-American Highway. The Highway, which is severely impacted by land sliding, is one of the main thoroughfares of Cuenca, with an estimated average daily traffic of 46,000 vehicles, per the Ministry of Transport and Public Works. The Pan-American Highway's closure cuts off a number of significant population centres, causing a crisis in road communications that severely impacts the population's mobility and the economy.

To reduce the risks connected with TIS failure, condition assessment, monitoring, and landslide early warning systems are becoming increasingly important and are driving the development of novel observing technologies and solutions (e.g., refs. [9,10]). In particular, early warning systems can include a combination of assessment, monitoring, prediction, and communication elements [11,12].

Regular visual inspections are the predominant method for Transportation Infrastructure Slope Monitoring (TISM), typically conducted every 2 to 10 years, contingent upon the Earthworks Hazard Category (EHC) system proposed by Network Rail, which classifies earthworks based on their statistical likelihood of failure from categories A to E with A statistically least likely to fail, and E the most likely to fail [8]. Continuous in situ measurements and monitoring [13] are other methods of conducting an earthwork examination. These methods are intended to detect and document signs of ongoing and developing instability in a consistent and repeatable way. More recently, early warning technologies have significantly advanced the field of TISM. These technologies not only facilitate the measurement of critical soil parameters but also enhance communication by providing timely information regarding potential anomalies that could lead to catastrophic events [14]. The early warning systems can use integrated geophysical and geotechnical methods, remote sensing, and rainfall monitoring. Geotechnical measurements from inclinometers, tiltmeters, piezometers, soil moisture sensors, and strain gauges in ground-based monitoring systems detect the changes in slope soil moisture, deformation, and slope movement. However, these geotechnical early warning systems are constrained in terms of coverage and scalability [15,16] generally, with intrusive investigations and point sensors, so only a very small proportion of a geotechnical asset can be directly monitored [17]. Likewise, in heterogeneous ground conditions, the discrete, single-point data provided by

these methods can be insufficient to assess the kinematics and behaviour of ground deformations. These challenges in obtaining spatial and continuous information on displacement patterns still exist, even if instrumental and topographic measurements are made across extensive networks [17,18].

On the other hand, remote sensing technologies (satellite, airborne, or drone-based) can address some of these limitations by identifying the changes in slope elevation and displacement, and other factors such as shallow soil moisture and vegetation health. However, there are challenges associated with these approaches as well, including the processing and interpretation of very large data sets [19], cloud cover affecting satellite visibility, limited spatial resolution [15,20] especially regarding smaller slopes [21], and the high cost for some techniques [22,23]. Recently, some challenges, particularly associated with big data handling, are being solved using artificial intelligence (AI) and deep learning [24–26]. On the other hand, remotely sensed data are generally only sensitive to the ground surface or very shallow subsurface and therefore cannot provide enough information on the subsurface precursors to slope failure especially for rainfall-induced landslides. According to refs. [27–35], landslides are strongly influenced by rainfall. The real-time monitoring of rainfall intensity and duration by rainfall monitoring systems can send out warnings when the rainfall surpasses crucial thresholds [36] that could cause landslides by setting thresholds based on past data [37,38]. However, there are limitations in using rainfall data alone to predict the precise position [39] and time of landslides. Moreover, the subsurface ground conditions, such as infiltration and drainage pathways, as well as the effects of evapotranspiration, play a critical role in rainfall-induced slope failures that cannot be directly determined from rainfall data alone.

To address some of the limitations of conventional investigations, remote sensing, and geotechnical monitoring, there has been a growing interest in the development and application of geophysical approaches in TISM (e.g., refs. [11,40–43]). Near-real-time information delivery, slope-scale subsurface models, spatial/volumetric subsurface data, and minimally invasive imaging are some of the main advantages of geophysical monitoring for slope stability applications [44].

While many reviews have discussed the geophysical applications for general landslide monitoring [11,41,45–49], a clear gap remains regarding slopes associated with transportation infrastructure. Instability in these slopes poses distinct challenges, such as high human and economic risks, limited accessibility, and specific engineering constraints. This review addresses that gap by focusing specifically on the advances in the development and application of geophysical methods for TISM.

This paper provides a novel, integrated overview of how geophysical methods contribute uniquely to the study of transportation slopes—such as those alongside roads, railways, and canals: 1. What geophysical methods have been successfully used for TISM? 2. What subsurface properties and structures can these methods reveal? 3. What monitoring and survey designs have been adopted for transportation slopes in terms of sensor deployment and the duration of measurements? 4. What are the benefits and challenges of the various geophysical approaches in this context? 5. What is the potential for the integration of geophysical and other techniques? 6. What are the main emerging technologies and research directions in this field?

2. Slope Instability Conditions and Indicators

Monitoring landslide precursor factors by using geophysical methods for TISs has been well developed in literature. Recent studies have shown that electrical imaging [50,51], seismic methods [52–54], and unmanned aerial vehicles [50] can be successfully applied to identify the TIS precursors to failure. Recent studies have demonstrated that electrical imag-

ing (e.g., refs. [14,43]), seismic methods (e.g., refs. [55–57]), ground penetrating radar (GPR) (e.g., refs. [58,59]), electromagnetic (EM) techniques (e.g., refs. [59,60]), and Distributed Acoustic Sensing (DAS) (e.g., refs. [61,62]) can be effectively applied to identify and monitor the precursors to failure in TISs. Besides the precursor factors, geophysical methods also can monitor the past failure conditions in TISs [14,43]. Figure 1 is an illustration of the slope instability conditions and indicators regarding TISM: the key features include tension cracks at the crest, rainfall effects, freezing–thawing cycles, vegetation impacts, a visible groundwater table, and a landslide.

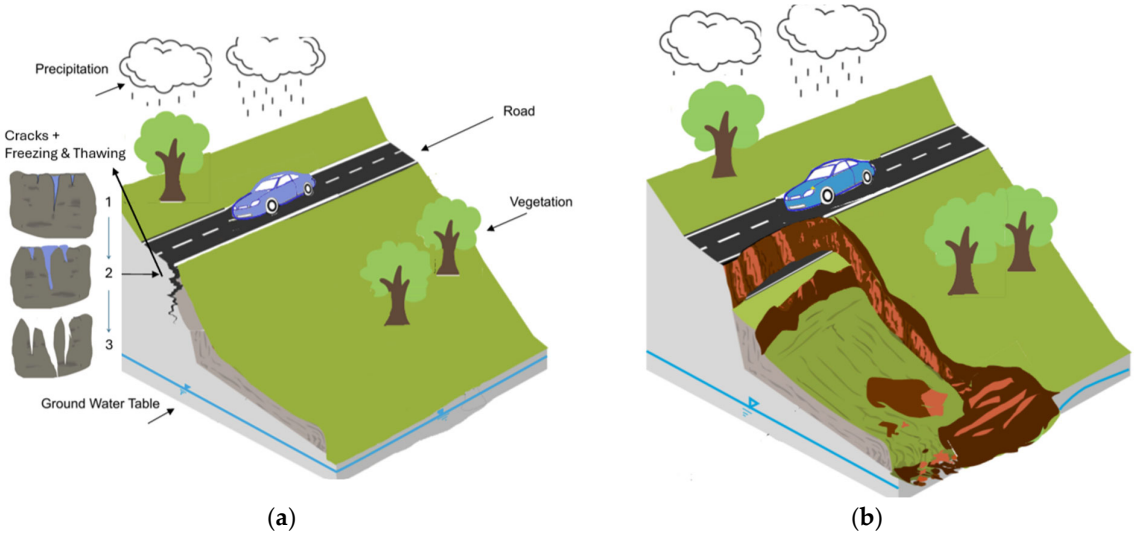

Figure 1. Illustration of slope instability conditions and indicators: key features include tension cracks at the crest, rainfall effects, freezing–thawing cycles, vegetation impacts, a visible groundwater table, and a landslide. (**a**) Pre-failure, (**b**) post failure.

2.1. Pre-Failure Condition

Pre-failure slope conditions in TISs involve a range of interacting factors, including seasonal and daily environmental variations, soil properties, and external influences. These factors contribute to the complex dynamics of embankment stability.

2.1.1. Seasonal and Environmental Variations

Freezing and thawing cycles significantly impact the mechanical properties of soft rock and soils. An increased moisture content reduces the cohesion and internal friction angle of soft rock, leading to a rapid decrease in slope stability. The cyclic action of freezing and thawing exacerbates soft rock fractures and fragmentation, further destabilizing TISs. Ref. [63] noted that the slope stability coefficient decreases exponentially with successive freezing–thawing cycles in TISs, especially in moisture-rich soils. Similarly, ref. [64] highlighted that in permafrost regions, the retention of freezing water and its subsequent melting contribute to transportation slope instability.

Wetting and drying cycles affect slope deformation, especially when pre-existing cracks are present. The interaction of processes such as freezing–thawing and wetting–drying cycles also amplifies the degradation of the geotechnical properties in soils. Refs. [65,66], demonstrated that these cycles dissolve cementing materials, increase the porosity, and weaken particle bonds, reducing the soil strength over time. In loess soils, wetting–drying weathering has a more pronounced impact than freezing–thawing cycles, highlighting the importance of considering the environmental conditions in stability assessments.

2.1.2. Influence of Cracks

Cracks facilitate rainfall infiltration into deeper soil layers, which increases the pore water pressure and reduces the shear strength. This influence varies depending on the crack orientation, intensity, and duration of rainfall. Studies such as [67,68] show that vertical cracks near the slope crest and those with a greater depth significantly reduce the safety factors and contribute to localized deformation, ultimately compromising slope stability.

2.1.3. Vegetation and Construction

Vegetation exerts both stabilizing and destabilizing effects on slopes. Ref. [69] found that while tree roots stabilize slopes, the weight of trees can cause destabilization, particularly on slopes with shallow soils. Ref. [43] observed that tree-induced seasonal fluctuations in soil moisture exacerbate the fissuring in clay-rich soils, reducing their shear strength. Conversely, grassy slopes are better suited for expansive soils due to their reduced shrink–swell effects. Construction activities, particularly on upslope areas, can activate dormant cracks and exacerbate instability by altering stress distributions and drainage patterns.

2.2. Partial Failure Conditions

Partial slope failures arise from a combination of factors such as topographical variations, soil disturbances, vegetation changes [70], and tensile cracks [71]. These elements influence localized instabilities. For example, the bending of trees, changes in vegetation cover, and varying soil types alter the stress distributions and hydrological conditions, potentially triggering partial failures.

2.3. Landslide Indicators Recognized by Geophysical Methods

Geophysical methods provide valuable tools for assessing landslide indicators, offering non-destructive and sensitive measurements of the soil and subsurface properties [51].

2.3.1. Cracks

Electrical resistivity techniques effectively characterize and monitor cracks in TISs as electrical properties are sensitive to the fracture size and distribution according to refs. [43,51]. GPR can detect internal cracks or hidden damage by analyzing the radar waves that bounce back from them. The application of GPR in monitoring the cracks associated with transportation infrastructures also has been studied by [51,72–74]. Seismic methods are also used for monitoring cracks in TIS by detecting stress changes. Cracks create variations in the soil properties, such as elastic and shear modulus, moisture content, and infiltration patterns [9].

2.3.2. Soil Disturbance

Geophysical methods, such as shallow seismic and ERT, analyze and capture the changes in the soil structure caused by the disturbances associated with landslides nearby transportation corridors [75]. Ref. [76] emphasized the utility of these methods in assessing the mechanical properties and hydrological impacts of disturbed soils.

2.3.3. Groundwater Conditions

Electromagnetic and electrical resistivity methods have long been used to investigate groundwater conditions, which significantly influence slope stability. These methods' sensitivities toward parameters, including fluid salinity and water content by measuring the resistivity values, enable them to monitor the hydrological dynamics of TISs [14,43,77,78].

By integrating multiple geophysical techniques with other traditional methods, researchers can monitor and detect slope failures more effectively, providing critical insights into the slope stability under varying environmental and geological conditions.

3. Geophysical Approaches Applicable to TISM

The evident importance of comprehending the spatiotemporal distribution of moisture content and stress in identifying the potential failures at the slope scale has prompted the broader development of geophysical systems for landslide monitoring. The sensitivity of resistivity measurements to moisture content complements the advances in some geophysical techniques, such as passive seismics for real-time event detection and active seismics to assess moisture-induced subsurface stress variations [51].

For transportation slope monitoring, four sub-categories of near surface geophysical methods are considered here: seismic methods; electrical methods; ground-based radar, such as ground penetrating radar (GPR); and electromagnetic (EM) methods. Various physical parameters, such as resistivity, density, or seismic velocities, can be determined using these techniques, either actively or passively. They can be used individually or in combination, depending on the specific slope assessment problem. Also, the choice of method depends on factors such as slope composition or the physical properties of the subsurface (material type), instrument costs and availability (acquisition set-up), and the desired penetration depth (level of accuracy and sensitivity [79]. Each of the geophysical methods has its own advantages and limitations. Geophysical methods' limitations include cost, sensitivity to the features of interest, signal to noise ratio, depth of resolution, and non-uniqueness of interpretation (e.g., ref. [80]). Integrated or multi-method surveys can reduce the uncertainties and bridge the gap between high efficiency and high-resolution structural information [59]. Based on the previously mentioned classifications, some of the most widely used geophysical methods for the assessment of unstable slopes are summarized in the following sections.

Figure 2 illustrates the various geophysical techniques utilized in monitoring slopes. These methods are categorized based on the type of information that they provide and their capability for real-time monitoring. Table 1 highlights each method's sensitivities to specific physical properties, subsurface conditions, and potential precursors to slope failure.

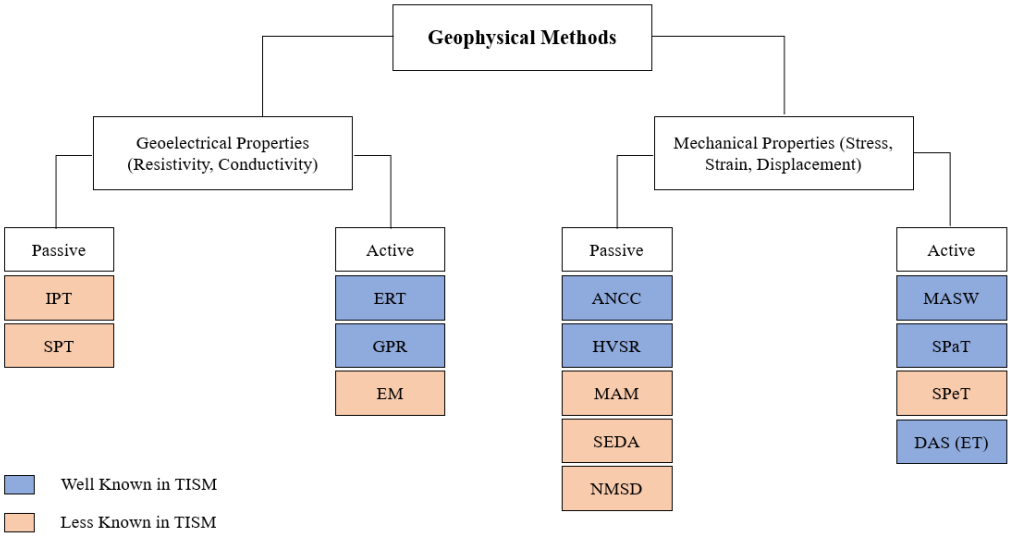

Figure 2. Geophysical techniques utilized in monitoring slopes. Acronyms used in this figure are defined below: EI—electrical imaging; ERT—electrical resistivity tomography; SPT—self-potential tomography; IPT—induced polarization tomography; SRaT—seismic refraction tomography; SReT—seismic reflection tomography; MASW—multi-channel analysis of surface waves; HVSR—horizontal-to-vertical spectral ratio; MAM—microtremor array measurements; ANCC—ambient noise cross-correlation; SI—seismic ambient noise interferometry; S-ANT—seismic ambient noise tomography; S-EDCL—seismic event detection, characterization, and location; NMSD—nano-micro seismic detection; DAS—distributed acoustic sensing; GPR—ground penetrating radar; EM—electromagnetic; ET—emerging technology; Vs —shear wave velocity; Vp—compressional wave velocity.

Table 1. Overview of geophysical methods with their directly measurable properties and inferred (indirect) parameters relevant to landslide and slope stability assessment.

Methods		Direct Properties	Indirect Properties
EI	ERT	Resistivity	Moisture content, groundwater salinity, pore fluid conductivity, stratigraphy, slip surface geometry
	SPT	Streaming potential	Subsurface fluid flow
	IPT	Polarization effect, chargeability	Moisture content, permeability, lithology, pore fluid chemistry
Seismic	SRaT (refraction)	Vp, and Vs	Moisture content, elastic properties
	SReT (reflection)	Vp, and Vs	Stratigraphy and discontinuities, elastic contrast
	MASW	Surface waves dispersion and Vs	Shear wave velocity (Vs), shear stiffness, stratigraphy
	HVSR	Fundamental resonance frequency (H/V spectral ratio)	Stratigraphy and thickness of layers, slip surface location, material strength
	MAM	Surface wave dispersion (via geophone array)	Stratigraphy, slip surface location, material strength
	ANCC (SI/S-ANT)	Travel time delays between correlated noise waveforms and dispersion curve	Subsurface structure, temporal changes in velocity (failure precursors), S-wave velocity, 2D/3D imaging
	S-EDCL/NMSD	Seismic event timing, frequency, amplitude, and location	Deformation precursors, displacement rate (via slidequake frequency)
	DAS	Distributed strain rate, seismic wave propagation time-lapse acoustic and vibration signals	Event type classification, source location sensitivity (qualitative), ground movement
	GPR	Subsurface reflections from material interfaces (e.g., bedding planes, cracks),	Hydrodynamics of the near surface, pore water pressure
	EM	Electrical conductivity, groundwater salinity, moisture content, water table depth	Saturation levels (inferred from conductivity), Clay content (inferred from conductivity variations), geometric boundaries of landslides

3.1. Electrical Imaging (EI)

EI has been widely applied in TISM, providing detailed insights into slope instability by imaging the key subsurface characteristics associated with landslides and ground movements [14,43,56,57,81–83]. Electrical properties are sensitive to key characteristics that can influence slope stability. These include the subsurface structure, clay content, porosity, and saturation and relate to hydraulic conductivity and permeability. EI can also indirectly assist in calculating important geotechnical parameters, such as those defined by the Mohr–Coulomb Failure Criterion, including the shear strength, pore water pressure, cohesion, and friction angle—all of which are crucial for understanding landslides [43]. EI can be split into three broad subgroups: Self-Potential Tomography (SPT), Induced Polarization Tomography (IPT), and Electrical Resistivity Tomography (ERT) [84]. Table 2 summarizes the research on TISM using EI methods conducted over the past three decades, highlighting the predominant use of ERT compared to other EI methods.

Table 2. A summary of research on TISM using EI. Note: "-" = not specified; "×" = multiplication.

Reference	Method	Monitoring Period (Days)	Monitoring Type	Grid Geometry	Survey Detail
Gunn et al., 2016; Gunn et al., 2018 [56,57]	ERT	270	Perm	2D	Two electrode lines, one parallel to the embankment, containing 96 electrodes spaced at 1.5 m. Another line, with 32 electrodes spaced at 1 m, ran over the embankment. A dipole–dipole configuration.
Gunn et al., 2015 [55]	ERT	180	Temp	2D	A profile (140 m) of 64 electrodes; electrode spacing of 1.5 m; parallel to the embankment transect. Several 32-electrode line arrays across the embankment; electrode spacing 1 m. Dipole–dipole electrode configuration.
Gunn et al., 2015 [55]	ERT	515	Perm	3D	Twelve cross-axis ERT lines, profile spacing of 2 m; electrode spacing of 1 m. Additional 32-electrode line arrays along the embankment; electrode spacing of 1 m. Dipole–dipole array configuration.
Holmes et al., 2020 [14]	ERT	720	Semi Perm	3D	Two electrode profiles. One ERT line (91 m) with 45 electrodes. The other ERT line (54 m) with 27 electrodes; electrode configuration of Wenner.
Su et al., 2021 [85]	ERT	120	Semi Perm	2D	Three longitudinal ERT profiles and three transverse ERT profiles were gathered. Each profile contained 32 electrodes and was 126 m long; electrode spacing of 2 m. Elec. config. of Schlumberger.
Chambers et al., 2014 [86]	ERT	840	Perm	2D & 3D	Within a 22 m portion of the embankment, a permanent ERT monitoring array was erected, consisting of twelve wires that ran perpendicular to the rails and were spaced 2 m apart. There were 32 electrodes on each line, spaced 1 m apart.
Chambers et al., 2022 [87]	ERT	720	Perm	4D	Two sensor arrays made up the installation: one was 91 m long and had 45 evenly spaced underground rod electrodes, while the other was 54 m long and had 27 evenly spaced buried rod electrodes.
Holmes et al., 2022 [43]	ERT	720	Perm	4D	Buried stainless steel rod electrodes were laid out in five lines, two of which ran uphill and three of which ran downhill, spanning a relict landslide and parts of un-slipped cutting on either side. Lines 1 and 2 had 91 electrodes spaced 1 m apart, whereas Lines 3, 4, and 5 had 19 electrodes.
Huntley et al., 2019 [81]	ERT	147	Perm	2D	Wenner configuration. Two intersecting ERT profiles: one 91 m with 45 evenly spaced electrodes, the other covered 54 m containing 27 electrodes.

Table 2. *Cont.*

Reference	Method	Monitoring Period (Days)	Monitoring Type	Grid Geometry	Survey Detail
Huntley et al., 2019 [59]	ERT	31	-	2D	One ERT line, Wenner array of 47 ground electrodes spaced every 5 m. Four ERT lines. A reverse Wenner array was used with a minimum electrode separation of 10 m.
Hen-Jones et al., 2017 [88]	ERT	720	Semi Perm	2D	The resistivity test chambers had interior dimensions of 78 mm × 25 mm × 25 mm, pin electrode separations of 25 mm and 75 mm, and were placed into the specimens at a depth of 5 mm. In accordance with the Wenner approach, a four-point drying curve was generated.
Chambers et al., 2022 [87].	ERT	~720	Perm	3D	Five ERT lines, two ERT lines across the slope, 91 electrodes, elec. spacing of 1 m, and three ERT profiles along the slope, 19 elecs., elec. spacing of 1 m. Measurement sets were acquired automatically once every 12 h using a dipole–dipole array configuration.
Tohari et al., 2017 [89]	ERT	~90	Perm	2D	Five ERT profiles, two parallel to the rail track and three across to the tracks, with a Schlumberger array configuration with an inter-electrode spacing of 5 m. No info about the number of electrodes in each profile and nothing about electrode or profile spacing.
Maleki et al., 2024 [90]	ERT	720	Perm	4D	Ten ERT profiles 3 m apart, each line with 24 electrodes – 240 electrodes in total, spaced 0.75 m apart.
Maleki et al., 2024 [90]	ERT	720	Perm	4D	One long ERT line with 256 electrodes installed across the slope, spaced at 1.3 m intervals
Glendinning et al., 2014 [91]	ERT	300	Perm	2D	Two 64-electrode arrays, 0.5 m spacing, dipole–dipole config., AGI Super Sting R8/IP instrument.
Gunn et al., 2015 [55]	ERT	~900	Perm	2D	ALERT system, 64 electrodes, 0.5 m spacing across 32 m, dipole–dipole config.
Calamita et al., 2023 [82]	ERT	300	-	2D	Five profiles: 710 m/470 m/141 m, electrode spacing 3–10 m. HVSR with three-comp. geophones, MAM with 24 synchronized sensors.
Moradi et al., 2021 [92]	ERT	~810	Temp	2D	ERT profile containing 96 electrodes, 0.5 m spacing, dipole–dipole configuration.
Gunn et al., 2015 [55]	ERT	~900	Perm	2D	Dipole–dipole config. ERT profile made of 64 electrodes, 0.5 m apart, covering 32 m.
Palis et al., 2017 [93]	ERT	365	Temp	2D	A total of 48 electrodes; 5 m intervals. A dipole–dipole config.
Harba and Pilecki, 2017 [94]	ERT	239	Perm	4D	One 224 m ERT profile with varying electrode spacing (1 m in the center, increasing toward the edges)

Table 2. *Cont.*

Reference	Method	Monitoring Period (Days)	Monitoring Type	Grid Geometry	Survey Detail
Colangelo et al., 2006. [95].	SPT	1	Controlled test	2D	Eleven electrodes separated by 5 m. A 50 m profile. The 24 h monitoring phase was a part of the longer semi-permanent monitoring campaign.
Perrone et al., 2004 [96]	ERT	-	-	2D	A 32-electrode system, electrode spacing of 10 to 30 m; a dipole–dipole array arrangement. During the field survey, eight ERT lines with lengths varying from 310 to 600 m were undertaken. Seven lines were oriented transversely to the landslide body; one line was oriented parallel to the accumulation zone. A total of 323 measurements were recorded for each profile.
Montgomery et al., 2022 [97]	ERT	600	-	3D	Two linear arrays with 64 electrodes each, each ostensibly located 2 m apart, making up the ERT system. A dipole–dipole array configuration was used.
Eulilli et al., 2015 [98]	ERT	-	Temp	2D	Two ERT profiles; the Wenner-Schlumberger array and the pole–pole array were the two types of electrode arrays used in this study. The "Super-Sting R8" multi-electrode resistivity system was used.
Su et al., 2023 [60]	ERT	342	Temp	2D	A dipole–dipole arrangement was used. There were 64 electrodes, 6 m spacing.
Nobahar et al., 2023 [50]	ERT	~2	Temp	2D	Multiple lines of 2D ERI surveys focusing on post-failure forensic evaluations, dipole–dipole array with 56 electrodes spaced at different centre-to-centre distances.
Chambers et al., 2021 [99]	ERT	365	Perm	2D	A linear array of 100 sensors over a distance of 200 m, with spacings between electrodes of 1–2 m.

Projects categorized by type—white represents rail projects, grey represents road projects, and blue represents canal projects.

3.1.1. Self-Potential Tomography (SPT)

SPT is a passive method based on the electrokinetic mechanism, where the movement of fluids or electrolytes in the subsurface generates electrical potential. Due to the chemical interactions between the mineral surface and porewater/fractured water, the soil particle surfaces are typically negatively charged [100]. The negatively charged mineral surface draws counter ions from porewater to form a layer known as the Stern layer [100]. The excess electric charges are then dispersed throughout the diffuse Gouy–Chapman layer. SPT can investigate rainfall-induced landslides, especially in situations where it is not possible to monitor the subsurface flows from the ground surface or landslip scars directly [100]. In the context of TISM, there is a limited number of published studies that have utilized SPT [95].

3.1.2. Induced Polarization Tomography (IPT)

IP is a polarization phenomenon, most commonly observed in areas containing scattered metallic particles (e.g., pyrite or magnetite), clay, or graphite. Although traditionally used in mineral exploration, IP techniques also hold relevance for environmental investigations, particularly in hydrogeophysical applications [84]. According to ref. [101], lithology, pore fluid chemistry, and water content all influence IP, offering strong potential for hydrogeophysical applications. The IP method has been applied by ref. [102] to characterize the critical subsurface material properties, such as permeability, water content, and clay content, in relation to transportation infrastructure slopes. A limited number of researchers have used IPT for TISM (e.g., ref. [103]). The landslide dynamic was investigated by ref. [103] using time-lapse time-domain induced polarization combined with ground-based imaging techniques.

3.1.3. Electrical Resistivity Tomography (ERT)

ERT directly addresses the soil properties that are critical for slope stability—parameters that are often more indicative of landslides—making it better suited for TISM. The method estimates the subsurface parameters by first measuring the apparent resistivity and then deriving the true resistivity distribution through an inversion process. These parameters include pore fluid conductivity, moisture content, porosity, groundwater salinity, mineral and geological boundaries, subsurface structures, flow pathways, and temperature variations [104]. Other landslide properties, such as sliding body thickness, lateral extension, depth, and temporal and spatial changes in the water content, can also be identified via ERT [105,106].

Increased moisture, often caused by rising rainfall, is one of the main causes of landslides worldwide. The moisture content in the ground is the primary factor influencing the pore water pressure, which affects the effective stress on a potential failure plane in soil or rock [107]. Effective stress, along with the cohesive properties of the slope material and the internal friction angle, determines the stability of a slope. ERT has been widely used for hydrogeological investigations [108]. The outcomes showed that during irrigation, ERT could precisely identify soil horizons and track the transport of soil water.

A single system can use hundreds of inexpensive electrodes (or sensors), and battery-powered instruments can perform active measurements. This approach contrasts with many other geophysical methods where the high cost of sensors limits long-term geophysical imaging or necessitates mobile or high-energy sources [109]. Moreover, ERT technology can be easily customized for applications requiring longer-term monitoring [110]. Acquiring repeat resistivity measurements can produce 4D models (i.e., time-lapse 2D or 3D) that reveal how properties, particularly the moisture content, vary both spatially and temporally. Time-Lapse Electrical Resistivity Tomography (TL-ERT) has been used as early as 2006 to assess the hydrogeological behaviour of landslides and characterize their internal structure (e.g., refs. [111,112]). It remains one of the most widely used geophysical methods for the long-term monitoring of landslides [11,14,43,44,51,81,86,88,112–115].

Automatic, multichannel measurement equipment and autonomous processing algorithms enable near-real-time ERT monitoring [116,117]. Monitoring studies where data are acquired on hundreds of electrodes within short timescales require careful consideration with respect to the survey design [115]. Efforts are made to restrict the quantity of data without lowering the information content. Repeated measurements can track the changes in the subsurface properties over time using time-lapse inversion, and comparing the resistivity distributions from several surveys carried out at different intervals [113]. The time-lapse geophysical monitoring of landslides is an area that has grown rapidly in the last decade or so [118].

An important consideration is that ERT measurements are also contingent upon the spatial arrangement of the electrodes. If these are not known accurately or if they move during monitoring due to slips, the resulting tomographic images can be distorted [119,120]. Surveying the electrodes' positions with suitable accuracy and frequency to match the ERT data sampling would be impractical and expensive. However, it is possible to obtain electrode position information from geo-electrical measurements by using suitable inverse methods [119,120]. These methods are applicable for either 2D or 3D ERT to recover position displacements on lines or grids of electrodes.

3.2. Seismic Method (SM)

Seismic methods are applied to investigate the seismic velocity propagation of the subsurface, providing valuable insights into subsurface structures, heterogeneities, and underground mechanical properties. Depending on how seismic waves interact with subsurface structures or boundaries, seismic methods can broadly be categorized into body wave methods (e.g., reflection and refraction) and surface wave methods. These methods traditionally utilize geophones or microtremors to detect seismic energy by converting the ground motion into digital information [121].

Seismic methods can also be categorized based on their energy sources: active methods and passive methods [45]. According to refs. [122,123], seismic reflection and seismic refraction are commonly used geophysical techniques for shallow subsurface studies. However, the vertical resolution of seismic reflection often lacks the submeter precision required for many real-world engineering applications. Surface wave methods, such as MASW, have proven to be reliable for detecting anomalies in the shallow subsurface and providing shear wave velocity (Vs) information [124].

Seismic methods can reveal the details about the soil physical characteristics, such as Vs, Vp, shear modulus (G), Poisson's ratio (ν), porosity (ϕ), Seismic Velocity Ratio (Vp/Vs), bulk modulus (K), and constrained modulus (M). Researchers have established connections between seismic measurements and geotechnical characteristics through petrophysical relationships and regression analysis, enabling the estimation of the porosity, stiffness, and saturation levels in clay soils [125]. According to ref. [126], other subsurface properties including moisture content, density, and shear strength can be derived from the velocity profiles of P- and S-waves. Seismic methods are conventionally used as manually deployed static survey techniques and are not commonly used for time-lapse monitoring of the subsurface. This is likely attributed to the limitations of the conventional seismic acquisition hardware, arising from the poor spatial coverage of conventional cables, as well as the costs associated with the required equipment, such as nodal geophones. Yet, recent advances in the use of Distributed Acoustic Sensing (DAS) has the potential to overcome some of these limitations, including the poor spatial and temporal resolution, enabling cost-efficient and high-resolution applications [54]. The application of DAS in monitoring slope instability is further discussed towards the end of Section 3.2. Table 3 describes real projects using seismic methods which demonstrate extensive use of MASW, as well as CSW, for monitoring slopes associated with railway, road, and canal infrastructures. Also, Table 4 provides real-world conducted projects that demonstrate the increasing use of FOC in TISM.

Table 3. A summary of research on TISM using SM. Note: "-" = not specified; "×" = multiplication.

Reference	Method	Monitoring Period (Days)	Monitoring Type	Grid Geometry	Survey Detail
Gunn et al., 2016; Gunn et al., 2018 [56,57]	MASW CSW	270	TEMP	2D	CSW: seismic source: a controlled frequency vertical oscillator containing up to six geophones (4 Hz) conducted across the crest of the embankment and just below the toe of the flanks. Wavelengths ranged from 0.3 m to 15 m, depending on the spacing of the geophones. The CSW method generated frequencies from 5 to 200 Hz. The horizontal sampling between CSW locations was 10 m. MASW: Coverage along 140 m by moving successive geophone arrays along the embankment. Seismic source: an impulsive sledgehammer and long geophone arrays (between 24 and 36 geophones). The frequencies generated were limited to below 80 Hz, but still allowed the characterization of the shallow subsurface. Geophones were spaced at either 0.5 m or 1 m, covering distances of up to 35 m.
Gunn et al., 2016 [56]	CSW MASW	-	-	2D	CSW: Five profiles of CSW, each containing 13 geophones with 1 and 2 m intervals, measuring signal frequencies up to 200 Hz. CSW surveys were undertaken along a 140 m section of the embankment, at the same stations with MASW and were laid out to complement the MASW survey line. Seven profiles, five of them parallel to the embankment crest; two crossed the embankment. MASW: Three profiles of MASW each containing 13 geophones with 1 m spacing intervals. Signal measuring was limited to frequencies below 100 Hz. MASW surveys were undertaken along a 140 m section of an embankment. Static arrays, with geophone spacing of 1 m.
D. Gunn et al., 2016 [56]	CSW MASW	~120	Temp	2D	MASW: Signal measuring limited to frequencies below 100 Hz. Source: 24-channel land streamer (4.5-Hz), geophones 1 m apart. A 300 m survey line divided into 50 increments, each covering 6 m. Rayleigh wave generator: a hammer/plate source, 2 m away from the nearest geophone. CSW: Measuring signal frequencies up to 200 Hz.

Table 3. *Cont.*

Reference	Method	Monitoring Period (Days)	Monitoring Type	Grid Geometry	Survey Detail
Gunn et al., 2015 [55]	MASW CSW	-	Temp	2D	MASW: Source: 14 lb hammer and plate. Survey along 130 m embankment axis, a series of static arrays with a 1 m geophone spacing. A total of 24–36 channel arrays of vertically polarized geophones that were spaced either at 0.5 m (array length up to 17.5 m) or 1 m (array lengths to 35 m). Also, land streamer 24-channel arrays of vertically polarized geophones. CSW: A 130 m survey along the embankment axis; 13 geophones. CSW survey stations were planned with respect to the MASW survey line. Signal frequencies up to 200 Hz were measurable using CSW whereas MASW was often limited to frequencies below 100 Hz.
Bergamo et al., 2016b [127]	Vp refrac-tion	180	-	1D (plus time)	The recording array used in all nine acquisition operations was set up with 24, 4.5 Hz, spike linked, vertical geophones spaced 2 m apart along a straight line on the embankment's crest. A 4.5 kg sledgehammer striking a metal plate was the cause of the seismic event. Along the seismic line, the source was positioned at 16 distinct points. To obtain seismic sections with a higher signal-to-noise ratio, three recordings were taken for each of these source points and then stacked in the time domain.
Bergamo et al., 2016a. [128].	MASW	480	-	2D	The MASW data were collected utilizing a land streamer made up of 24 vertical geophones with 4.5 Hz along the embankment crest. The geophones were mounted to the ground using cleated metal plates and spaced at 1 m intervals. A 4.5 kg sledgehammer striking a metal plate 2 m away from the first receiver served as the seismic source. In most cases, a total acquisition time of under 2 h was achieved.
Yang et al., 2022 [129]	AN	-	Temp	1D	Triaxial accelerometers on ground/slope points, 2–8 m apart, frequency range 0.2–10 Hz.
Calamita et al., 2023 [82]	HVSR MAM	300	-	1D	Five profiles: 710 m/470 m/141 m, electrode spacing of 3–10 m. HVSR with three-comp. geophones, MAM with 24 synchronized sensors.
Liu et al., 2023 [130]	HVSR	60	-	1D	Sixteen locations in the sliding zone; DATAMARK JU410, 15 min records, 100 Hz sampling.

Table 3. *Cont.*

Reference	Method	Monitoring Period (Days)	Monitoring Type	Grid Geometry	Survey Detail
Palis et al., 2017 [93]	AN	365	Temp	2D	A permanent seismological array, continuously recording microseismic events since 2010 at the station. This setup included six vertical velocity sensors placed 50 m from a central three-component 4.5 Hz velocimeter, with all the sensors buried at a depth of 1 m and connected to a receiver. The ambient seismic source included rockfalls and internal quakes.
Imposa et al., 2017 [131]	MASW, AN	2	Temp	2D	MASW: active: two active MASW surveys: December 2010 and April 2015, an array of 12 vertical geophones (4.5 Hz) 4 m and 5 m apart. The energy source of a weight drop was used, and multiple energizations were performed about 8 m from the geophone starter to enhance the signal's energy content relative to ambient noise. AN: three-component microtremor, 16 min recording duration, 128 Hz sampling frequency. Five HVSR sections were acquired using four compact tomographs (1 dm^3, 1 kg, 2200 V/(m/s) sensitivity, 24 dB, 0.1250 Hz resolution). Environmental noise was recorded at each station for 16 min to ensure signal stability at the 128 Hz sampling frequency.
Harba and Pilecki, 2017 [94]	S-ANT	3	Temp	2D	Noise source: high-frequency seismic noise from heavy vehicular traffic on a nearby road. Two intersecting profiles (75 m and 95 m in length) were surveyed using twelve seismometers spaced 10–20 m apart. Recordings lasted 60 min, with a sampling interval of 10 ms and a frequency range of 0.03–100 Hz.
Brückl et al., 2013 [132]	AN	212	Perm	1D	Six Geospace GS-11D 4.5 Hz three-component geophones monitored the seismic activity across the GMM. Unique seismic events included the following: short, high-frequency bursts (up to 100 Hz); longer, lower-frequency events (<60 Hz); low-amplitude, narrowband, lasting 10–30 s; long (>60 s), low frequency (<50 Hz); high-frequency spikes on one station with corresponding low-frequency signals on others. A nearby reference station and sound sensors aided in distinguishing mass movement-induced seismic events from other sources.

Table 3. *Cont.*

Reference	Method	Monitoring Period (Days)	Monitoring Type	Grid Geometry	Survey Detail
Mainsant et al., 2012 [53]	SR S-CC	146	-	1D	Two active seismic profiles were performed along and across the landslide. The longitudinal profile used eight geophones at 5 m spacing with explosive shots, while the transverse profile used eight geophones at 8 m spacing with hammer strikes on a plate. Two 2 Hz three-component seismic sensors were buried at 40 cm depth, 35 m apart in stable terrain outside the landslide. Each sensor was connected to a 24-bit Kephren acquisition station, digitizing and storing data at 250 Hz.
Su et al., 2023 [60]	MASW	342	Temp	2D	A oll-along shear wave velocity imaging across the electrical profiles was performed using 24 geophones (4.5 Hz) spaced 2 m apart with an offset spacing of 4 m. Seismic source of a 10 kg hammer on a metal plate as a cut-off frequency, and the spectral analysis's dramatic amplitude fall around 110 Hz was chosen.
Gunn et al., 2016 [56]	CSW MASW	-	-	2D and 3D	CSW: Measuring signal frequencies up to 200 Hz. CSW surveys were undertaken along a 140 m section of the embankment, at the same stations with MASW and were laid out to complement the MASW survey line. Seven profiles, five of them parallel to the embankment crest; two crossed the embankment. MASW: Signal measuring limited to frequencies below 100 Hz. Four profiles, each parallel to the canal line, and each 17.5 m long; 36 vertical geophones with a series of overlapping eight-channel geophones, spaced at 0.5 m; MASW surveys were undertaken along a 140 m section of an embankment. Static arrays, with geophone spacing of 1 m.

Table 3. *Cont.*

Reference	Method	Monitoring Period (Days)	Monitoring Type	Grid Geometry	Survey Detail
Tonnellier et al., 2013 [133]	S-EDCL	10	SemiPerm	2D	One three-component sensor was surrounded by six one-component sensors in each of the two deployed tripartite sensor arrays. The seismic arrays used in passive seismic acquisition systems had a radius of 20 and 40 m. A tripartite-shaped array had one three-component (3C) sensor in the centre and six vertical sensors spaced roughly 20 and 40 m apart in each of the three directions. The upper portion of the landslide had two seismic arrays constructed. As the optimal trade-off between signal resolution, data storage, and data transmission, the data sampling rate was set at 400 Hz. For both locations, the ground motion was concurrently recorded on all channels of each array with a flat frequency response in the frequency range [2–80] Hz.

Projects categorized by type—white represents rail projects, grey represents road projects, and blue represents canal projects.

Table 4. A summary of research on TISM using FOC. Note: "-" = not specified; "×" = multiplication, and DSS stands for Distributed Strain Sensing.

Reference	Method	Monitoring Period (Days)	Monitoring Type	Grid Geometry	Survey Detail
Xie et al., 2024 [134]	FOC (DAS)	-	Temp	3D	Array in shallow trenches (30 cm deep), fully armoured sensing cable. DAS parameters: 1 m channel spacing, 10 m gauge length, 1000 Hz rate. Seismic sources: strikes on a thick 40 mm plate at seven different distances from the midpoint of the trenches. Additional sensors: eight three-component nodal seismic stations deployed near the FOC array for reference, sampled synchronously with the DAS unit.
Moore et al., 2010 [61]	FOC (DSS)	420	Temp	2D	Two types of sensors: one chain of three borehole sensors (at depths of 38, 40, and 68 m; extending up to 20 m), and two surface extensometers (measure both strain and temperature). Data collection in two modes: (a) dynamic measurements (triggered by deformation) at high sampling rates (100 Hz). (b) Static data logging every 5 min.

Table 4. *Cont.*

Reference	Method	Monitoring Period (Days)	Monitoring Type	Grid Geometry	Survey Detail
Kang et al., 2024. [83].	FOC (DAS)	45	-	2D	A 10 km dark fibre parallel to the road and rail line (perpendicular to the slope); a gauge length of 8 m; a channel spacing of 4 m; a sampling frequency of 200 Hz.
Moore et al., 2010 [61]	FOC (DSS)	420	Perm	1D	One chain of three borehole sensors, and two surface extensometers. Dynamic measurements (triggered by deformation) at high sampling rates (100 Hz). Static data logging every 5 min.
Kang et al., 2024 [83]	FOC (DAS)	45	-	2D	A 10 km dark fibre; a gauge length of 8 m; a channel spacing of 4 m; a sampling frequency of 200 Hz.
Brückl et al., 2013 [132]	FOC (DSS)	212	Perm	2D	Six three-component geophones of 4.5 Hz monitored the seismic activity across the GMM. Unique seismic events included the following: short, high-frequency bursts (up to 100 Hz); longer, lower-frequency events (<60 Hz); low-amplitude, narrowband, lasting 10–30 s; long (>60 s), low frequency (<50 Hz); high-frequency spikes on one station with corresponding low-frequency signals on others. A nearby reference station and sound sensors aided in distinguishing mass movement-induced seismic events from other sources.

Projects categorized by type—white represents rail projects, and grey represents road projects.

3.2.1. Active Seismic Methods

Active methods use controlled seismic sources, including a sledgehammer, weight drop, elastic wave generator, electromechanical vibrator, or explosive charges, to produce waves that are then recorded via sensors such as geophones [135]. Seismic Reflection Tomography (SReT), Seismic Refraction Tomography (SRaT), Continuous Surface Waves (CSW), and Multichannel Analysis of Surface Waves (MASW) are classified as active seismic methods [135].

- Seismic Refraction Tomography (SRaT)

SRaT is an active-source seismic technique, occasionally used for monitoring landslides. SRaT incorporates more shotpoints and receivers compared to traditional seismic refraction methods, enabling improved imaging [136]. By determining the travel times of artificially generated seismic waves, SRaT generates subsurface models of seismic velocity based on the first arrival times of P- and/or S-waves [137]. Vp is commonly employed to identify significant velocity differences between the landslide mass and the underlying bedrock [138–140]. By measuring Vp and Vs, SRaT can provide researchers with 2D or 3D images regarding the distribution of elastic properties of the subsurface. SRaT is sensitive to soil elastic properties, and moisture content variation which is one of the most important triggering parameters in landslide occurrences [137]. A critical limitation of SRaT is that it assumes a continuous increase in velocity with depth. Where this assumption fails, seismic reflection provides a clearer and more reliable imaging solution [124,141]. In recent years,

several researchers have utilized this method for characterizing TISs (e.g., refs. [138,142–145]. However, its application for TISM has been explored in only a limited number of studies (e.g., ref. [127]).

- Seismic Reflection Tomography (SReT)

SReT is another active seismic method which focuses on the elastic differences between two subsurface strata by measuring the relative travel times for different geophones. According to ref. [141], high-resolution seismic reflection profiling is an efficient technique for 2D or 3D visualization of the geometry of landslide structures and locating the subsurface discontinuities in TISs. Despite its high survey accuracy, high horizontal and vertical resolution, and large quantities of acquisition information that characterize the seismic reflection approach [146], SReT is not commonly used for near-surface investigations associated with TISs. Unlike SRaT, which assumes increasing seismic velocity with depth, SReT is well suited to imaging complex subsurface structures and velocity profiles, even in situations where velocities decrease with depth. The choice between these two methods depends on the geological context, resolution needs, and project constraints [124,141]. Although several studies have employed SReT for monitoring natural slopes (e.g., refs. [147–151]), their application in TISM remains notably limited due to the significant challenges associated with acquiring high-quality seismic reflection data in such environments.

- Multi-Channel Analysis of Surface Waves (MASW)

MASW is most associated with the analysis of Rayleigh wave propagation, from active sources such as a sledgehammer or weight drop (e.g., refs. [143,152]). MASW involves selecting dispersion curves from phase velocity–frequency spectra and inverting these curves to produce 1D and 2D subsurface shear–wave velocity (Vs) profiles. This information can reveal details on stratigraphy and shear stiffness [153]. Continuous Surface Waves (CSW) are used as another approach for measuring the surface wave velocity to determine ground stiffness. The CSW approach involves a smaller number of geophones (typically 4 to 6), in contrast to MASW, which utilizes a larger number of geophones (24 to 36 or more). The smaller number of receivers in the CSW approach makes it more suitable for analyzing a small section of the subsurface [56]. According to ref. [56], CSW can be used in higher-resolution studies which use a vertical vibrator with a controlled frequency source of seismic energy. MASW and CSW have been more commonly used in TISM compared to the other active seismic methods (e.g., refs. [56,57,128,131]).

3.2.2. Passive Seismic Methods

Passive seismic methods use ambient noise, either natural or human-generated background seismic energy [154]. The term “ambient noise” can include wind, trees, buildings, trains, roads, industrial machinery, waves, and footfall [155], and recent studies (e.g., refs. [156,157]) have demonstrated that ambient noise can serve as a reliable energy source for subsurface investigation. Several passive seismic techniques are used in TISM, including Horizontal-to-Vertical Spectral Ratio (HVSR), Microtremor Array Measurements (MAMs), and Nano-Micro Seismic Detection (NMSD). Other widely applied methods are seismic cross-correlation techniques, also known as Ambient Noise Cross-Correlation (ANCC), which include Seismic Ambient Noise Interferometry (SI) and Seismic Ambient Noise Tomography (S-ANT). In addition, Seismic Event Detection Approaches (SEDAs), such as Seismic Event Detection, Characterization, and Location (S-EDCL), may be utilized [154].

- Ambient Noise Cross-Correlation (ANCC)

Seismic Cross Correlation, which includes SI and S-ANT, uses natural and anthropogenic noise to correlate waveforms between different stations, focusing on the differences in travel times to study subsurface structures [158]. Landslide researchers (e.g., ref. [159])

became increasingly interested in this technique after studies including refs. [53] first identified a distinct decrease in velocity five days prior to a landslide event.

Both SI and S-ANT rely on continuously recorded seismic data, but an important distinction is that S-ANT can be used to generate tomograms, as highlighted in [11]. The process involves performing a frequency–time analysis on the outputs from cross-correlations to extract dispersion curves [160]. Dispersion curves can then be inverted to determine near-surface S-wave velocities (e.g., ref. [161]). The interpolation of these inverted dispersion curves between sensor pairs facilitates the creation of tomographic images. Linear sensor deployments typically yield 2D profiles, while nonlinear arrays have demonstrated the capability to produce 3D images, such as those used to map landslide bodies [162].

SI offers a promising approach to identify failures in recent landslide investigations (e.g., refs. [163–165]). S-ANT has also been used for several investigations into natural landslides (e.g., refs. [53,133,159,166,167]). However, to date, only a few studies (e.g., ref. [168]) have specifically examined the application of S-ANT for TISM.

- Horizontal-to-Vertical Spectral Ratio (HVSR)

The HVSR technique is another well-known passive seismic method, in addition to seismic cross-correlation methods, for obtaining dispersion curves. Unlike seismic cross-correlation, however, HVSR relies on data from a single seismometer. This approach measures three components of seismic noise to determine the fundamental resonant frequency associated with a subsurface layer boundary (soil–rock) at which there is a change in acoustic impedance. This resonance frequency is related to the layer thickness and the shear wave velocity of the layer [130,169].

Besides slope characterization [170], and instability mapping [167], HVSR can also be used to estimate the relative strength of different subsurface layers, detect and monitor the changes in layer thickness, and identify geological structures such as slip planes by analyzing the resulting spectral ratio curves [11]. As for slope monitoring, a few studies (e.g., refs. [82,130,171,172]) have specifically examined and approved the application of HVSR for TISM. However, HVSR mostly works well in areas where the ground is relatively uniform and has slightly inclined or horizontal layers, and where there is a clear difference in the mechanical properties between layers, allowing the sliding layer to resonate [45,173–175].

A recent development towards achieving ground amplification is to analyze through an array configuration of sensors instead of using only one seismometer (e.g., HVSR). While the HVSR technique considers only the spectral ratio at a single receiver, Microtremor Array Measurement (MAM) utilizes an array of geophones [130]. MAM analyzes the spatial distribution of waveforms to estimate surface wave dispersion curves [130]. Over the past few years, several studies have explored the application of MAM in landslide investigations, including works by refs. [82,176]. According to ref. [130], MAM is a reliable and highly effective geophysical method for detecting and monitoring susceptible slopes, such as those along transportation routes. Recently, studies including refs. [82,130,177] have advanced the application of MAM in TISM.

- Seismic Event Detection Approaches (SEDAs)

By continuously detecting, characterizing, and locating seismic events, Seismic-Event Detection, Characterization, and Location (S-EDCL) methods provide a detailed understanding of the internal state of the landslide and any signs of impending movements. It entails the direct interpretation of the signals captured by semi-permanent seismic sensors, either by identifying and categorizing seismic events related to movement in the landslide mass or by precursory activities that may be linked to impending movement (a phenomenon seen in rockfalls and other brittle landslides, or a response to recent increased infiltration [93,133]. This form of monitoring can be accomplished with a single seismic

sensor installation, but the detection of the location of observed events requires a network of seismometers. Studies involving rockfalls and other rapidly failing landslides frequently employ S-EDCL methods, because they are the only techniques that allow for the near-real-time identification and characterization of landslides at the regional scale [11]. In the context of landslide monitoring, S-EDCL can assist in real-time risk assessment, offering insights into the ongoing dynamics of a landslide. Some of the most recent studies on TISM using S-EDCL include refs. [93,178–180].

NMSD is another seismic event detection approach widely applied in studying landslide mechanics. It involves locating, identifying, and pinpointing weak energy signals known as "slidequakes", which are typically short in duration and characterized by discernible, traceable wave packets [181,182]. Slidequakes may also be produced as a result of rainfall-induced failure in the landslide mass [133,181–186]. NMSD can be remotely used to monitor slidequakes and afterslides, as well as to determine their size and timing [167]. The microseismic rate recorded via NMSD correlates with the displacement rate of landslides, serving as a proxy for displacement monitoring and enabling the prediction of the time to failure through displacement-based methods [167]. The successful application of NMSD in identifying smaller-scale events (failures) could play a vital role in preventing landslides in railway embankments [187]. Several recent studies including refs. [61,93,176,178,188] emphasize the importance of NMSD networks in early warning systems and TISM.

- Emerging Technologies—Distributed Acoustic Sensing (DAS)

DAS is a non-seismic method but capable of obtaining seismic data by detecting high-frequency waves using FOC [189]. By transmitting laser signals through a single-mode FOC and analyzing the backscattered light, DAS can measure time-lapse acoustic, vibration signals and changes in the local axial strain along the cable [190]. DAS is cost effective, and can make use of existing unused "dark fibers" originally installed for communication purposes [83]. DAS also offers high spatial and temporal resolution for near-surface monitoring, surpassing many other ambient seismic noise methods. DAS enables the remote monitoring of extensive track lengths, eliminating the need for dense sensor deployment or frequent manual inspections [54,191]. Although the application of DAS for active and passive seismic monitoring remains in its early stages, recent studies (e.g., refs. [54,191] have demonstrated its potential in monitoring earthwork slopes. The application of DAS for the early warning of landslides related to transportation assets has garnered significant attention (e.g., refs. [54,134,189,191]). This approach is especially promising for railway sites, where existing FOCs are already installed. These capabilities position DAS as a transformative technology for proactive landslide and rockfall monitoring along critical infrastructure. However, analyzing DAS data—especially in real time—can be challenging, since the signals from mass movements are often weak and difficult to detect.

3.3. Ground Penetrating Radar (GPR)

GPR is an active method, involving the propagation and detection of electromagnetic waves in the subsurface. These waves are generated by an antenna and are either absorbed or reflected by the features of the underlying material, such as cracks, moisture, and material interfaces or bedding [45]. The energy reflected by the surface irregularities is detected by a receiver, aiding in the creation of subsurface images. The subsurface images can track the hydrodynamics of the slope subsurface which is a key factor in landslide triggering [192]. GPR also can be used for the real-time monitoring of the pore water pressure [193] as opposed to traditional seismic methods which only obtain snapshots. The depth of the investigation varies from centimetres to tens of metres depending on the antenna frequency and the composition of the subsurface. A major limitation of the technique is signal attenuation in electrically conductive conditions, such as clay-rich or

water-saturated environments. (e.g., refs. [194,195]). Nevertheless, in favourable (e.g., electrically resistive) conditions, it provides a rapid means of providing high-resolution [122] time-lapse subsurface information [193]. According to ref. [193], two drawbacks of "classical" GPR, are that: (1) it cannot be utilized for automated monitoring, and (2) interpreting GPR observations becomes challenging in the absence of distinct gradients or reflectors, particularly when attempting to determine subsurface water content profiles. Table 5 presents real-world projects utilizing GPR in TISM, which shows that its usage has been sporadic over the years without significant periods of high activity.

Table 5. A brief summary of research on TISM using GPR. Note: "-" = not specified; "×" = multiplication.

Reference	Monitoring Period (Days)	Monitoring Type	Grid Geometry	Survey Design
Huntley et al., 2019 [59]	30	-	2D	Two surveys: Survey 1. A nominal source frequency of 100 MHz and 50 MHz antennae was used. The antennae were dragged over the slope with a fixed transmitter-receiver separation of 1 m. Continuous data collection was performed at a rate of approximately 15 soundings per second, allowing for the detailed mapping of the subsurface. Survey 2. A nominal source frequency of 30 MHz. The survey involved ten lines while travelling downstream in a raft.
Borecka et al., 2015 [58]	-	Temp	2D	Two GPR profiles with an antenna frequency of 100 MHz. Time windows: 600 ns and 800 ns; sampling: 1024; step: 20 cm.
Lissak et al., 2015 [196]	10,958 (1980–2010)	Perm	2D	RAMAC GPR system, shielded 500 MHz dipole antenna in a monostatic arrangement (transmitter and receiver in the same unit), multiple parallel GPR profiles across three cross-sections, 50–90 m long and 6 m wide, in-line sampling interval: 0.05 m, time window: 105 ns.

3.4. Electromagnetic (EM)

EM is an active technique sensitive to subsurface electrical conductivity (or resistivity). Compared to GPR, EM methods offer a greater penetration depth but a lower spatial resolution, operating at lower frequencies. EM surveys can be conducted rapidly from airborne/UAV or towed platforms without requiring ground contact, using transmitter and receiver coils. Time-varying currents in the transmitter generate EM fields that induce secondary currents in geological materials, which are then detected by the receiver coil, providing information on the subsurface electrical properties [121]. The significant benefit of the non-contacting operation of EM (e.g., a UAV-based EM tech) has been demonstrated in tests using an electromagnetic conductivity meter on landslides [197]. The EM approach can be applied similarly to ERT, if the frequency is low enough and the coil separation is much less than the skin depth. This approach offers an apparent conductivity value that is solely dependent on the ground resistivity and coil separation. When the depth of the material being studied is consistent, surveys can be completed more quickly, and the method can be preferred to a constant electrode spacing resistivity study [197].

For landslide assessment, EM methods can be categorized into different subgroups based on the specific techniques employed. Some of these subgroups include Time Domain Electromagnetics (TDE), Frequency Domain Electromagnetics (FDEM), Electromag-

netic Induction (EMI), and Magnetotellurics (MT). The effectiveness of these methods in identifying the geometric boundaries of landslides makes them invaluable for landslip analysis. FDEM is more commonly performed with two horizontal loops and a ground conductivity meter [198].

EM techniques are commonly applied to investigate groundwater salinity, porosity, permeability, electrical conductivity, dielectric permittivity, depth to the water table, mineral exploration, subsurface structures, and soil moisture content [199]. In EM measurement, the penetration depth varies depending on the coil separation [118]. This ability to measure and interpret a wide range of subsurface properties underscores the versatility and importance of EM methods in geological and environmental studies. Table 6 summarizes the research on TISM using GPR and its sporadic application with no significant period of high activity.

Table 6. A summary of research on TISM using EM. Note: "-" = not specified; "×" = multiplication.

Reference	Monitoring Period (Days)	Monitoring Type	Grid Geometry	Survey Detail
Su et al., 2021 [85]	120	TEMP	2D	Three TEM survey lines, measuring 126 m, 200 m, and 300 m in length, with a 10 m spacing between the measurement points. Emission frequency of 25 Hz, and emission current of 1 A. The transmitter coil had a side length of 2 m.
Huntley et al., 2019 [59]	360	2D	-	Two FEM surveys of 10 m and 2.5 m in the vertical dipole mode. Two acquisition modes of continuous and stationary points every 10 m. GPS integrated.

4. TISM Case Studies

Recent case studies show that geophysical approaches have been used for landslide detection and monitoring in transportation slopes, such as roads, rail networks, and canals. TISs generally refers to slopes that have been engineered, or maintained to support transportation systems such as highways, railways, or embankments associated with roads and bridges. Table A1 describes case studies on monitoring TISs using near-surface geophysical methods. The data demonstrates the extensive use of geophysical methods, including ERT, MASW, as well as FOC, for monitoring slopes associated with railway, road, and canal infrastructures. Both temporary and permanent monitoring setups were utilized, with temporary monitoring being more commonly employed. The data collection periods ranged from a single day in some studies to several years in others. The integration of different methods, tailored to specific sites and objectives, highlights the effectiveness of geophysical approaches in long-term and short-term infrastructure monitoring. The top one geophysical method used in TISM includes ERT, as well as FOC as an emerging technology which has also gained popularity in this regard.

Figure 3 highlights how frequently different geophysical techniques have been used in TISM studies over the past 15 years (2010–2024), based on the case studies cited in this manuscript. Among these, ERT and passive seismic methods stand out as the most used, with ERT seeing a rise in popularity in recent years. ERT usage has steadily increased since 2015, reaching a peak between 2017 and 2020. After 2020, its usage has remained steady, highlighting its broad applicability and reliability. Seismic methods, on the other hand, show peaks in 2015 and 2024 but then experienced a significant decline, possibly indicating losing interest.

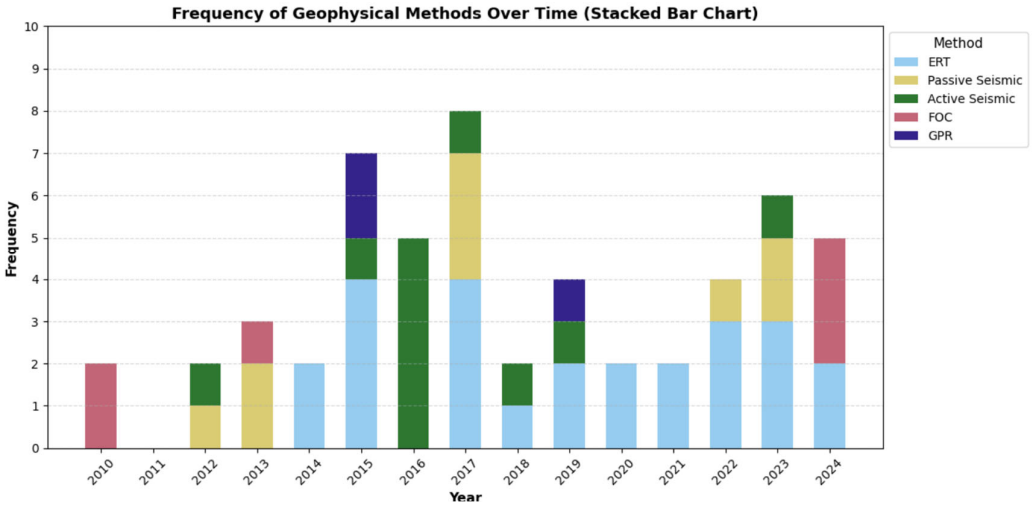

Figure 3. Frequency of published studies regarding TISM using different geophysical techniques over time.

Meanwhile, EM and GPR techniques have been used sporadically over the years without notable periods of high activity. FOC, as a newer technology, showed minimal use until a sharp rise in 2024, likely reflecting a growing interest or recent advancements that have made it more practical.

5. Strengths and Weaknesses of Geophysical Methods for Geotechnical Asset Condition Assessment

Geophysical methods have inherent limitations which has led to a focus on using combined techniques in landslide monitoring [200].

According to refs. [195,201], GPR is widely proven for providing remarkably high-resolution data, especially when employing 100 MHz antennae and particularly in shallow subsurface exploration. With its high-resolution output, GPR is capable of providing detailed information on the internal landslide structure and bedrock depth. GPR data can also be stored and analyzed later, facilitating advanced post-acquisition processing [202]. GPR outperforms other methods in detecting the soil dielectric permittivity, closely related to the soil water content [193]. GPR surveys are fast, economical, and minimally disruptive to ongoing transportation operations [74]. Data collection can be managed via mobile devices or cloud storage, enhancing accessibility and collaboration [74].

The rapid data acquisition and effective imaging capabilities of GPR in TISM (e.g., ref. [59]) are valuable, yet the method faces significant challenges in this field. GPR is vulnerable to external interferences such as those from radio transmitters and mobile devices, which can degrade the data quality [122,202]. High-conductivity materials like clay and saline water can cause rapid signal loss, limiting GPR's penetration depth and efficacy [122,203]. Near-surface reflections and energy loss can create misleading reflections in radar profiles, complicating the data's interpretation [122]. Elevation changes, antenna alignment issues, and velocity variations with depth can distort GPR profiles, requiring expert knowledge for accurate analysis [74,122]. Expertise is essential for processing GPR data, especially when interpreting soil water content (SWC) profiles, which may lack distinct reflections [193].

Seismic data can identify debris flows, slip surfaces, landslide material thicknesses, and monitor remote events like rockfalls [49,189]. Passive seismic data assist in analyzing the collapse kinematics, while ERT complements this by examining the moisture dynamics on unstable slopes [137].

Nevertheless, seismic methods can have noticeable challenges. Seismic methods are costly and require extensive data processing, which can be subjective and time intensive [97,141]. Traffic noise and rugged topography complicate data collection, while limited sensor deployment constrains spatial resolution [137]. Seismic data may not reflect seasonal variations, and microseismic signals can be misinterpreted if caused by external factors [204]. DAS struggles with seismic source localization due to signal attenuation, and conventional inversion methods do not adequately account for topographic influences [97,134].

ERT provides spatially detailed images and can monitor time-lapse changes in slope moisture, which is invaluable in landslide studies [137]. ERT's use of low-cost electrodes allows for long-term monitoring without prohibitive expenses, unlike other geophysical methods [109]. ERT has developed techniques to incorporate topography into resistivity inversion, improving the data accuracy in challenging terrains. It also has limitations. ERT struggles with non-unique solutions and depth limitations, especially in complex, three-dimensional landslide settings [80]. In soils with high water or clay content, resistivity contrasts can be weak, making interpretation difficult. This issue may be partially addressed by using induced polarization techniques [48]. ERT requires expensive hardware for deeper exploration, and limitations in automated processing hinder real-time data analysis [205].

Electromagnetic methods present a final, yet limited option for landslide monitoring. EM data are sensitive to data distortions, caused by geological noise, instrumental errors, and environmental interferences, and that require technical expertise for accurate interpretation [206]. The electromagnetic field's penetration is affected by the ground's magnetic, conductive, and dielectric characteristics, limiting the technique's applicability [206]. In geodetic surveys, EM positioning accuracy is constrained by air refraction effects, affecting surveys over long distances [207].

Despite these limitations, EM methods contribute specific advantages: they allow for quick survey execution, as they do not require electrode installation [118] and hence are suitable for quick-mapping applications.

Table 7 briefly compares four primary geophysical techniques used in landslide monitoring and emphasizes the limitations and strengths of each geophysical technique. Figure 4 demonstrates a summary of the geophysical methods' performance in TISM.

To overcome the trade-off between the advantages and limitations, ref. [48] recommended the joint application of geophysical techniques, such as GPR, ERT, and seismic tomography. As ref. [208] noted, GPR typically offers more valuable information on the shallowest strata, ERT does so for the intermediate layers, and seismic does so for the deepest layers [209]. The seismic approach can provide information on the displacement material more effectively than ERT if the material under investigation is extremely moist [48]. Therefore, while some methods focus on near-surface features, others address deeper subsurface structures, both of which are crucial for understanding the slope stability [210]. In TISM, integrating geophysical methods like SM, ERT, and GPR enhances cost efficiency and improves slope assessments. A study conducted by ref. [57] explores the use of multi-geophysical methods to enhance the predictive and preventative maintenance of railway infrastructure, focusing on ageing embankments. Using a combination of CSW, MASW, and ERT, the research developed a subsurface stiffness model and monitored dynamic groundwater behavior. Figure 5 illustrates the spatial deployment of the CSW, MASW, and ERT profiles along the monitored embankment. The CSW and MASW surveys characterized shallow subsurface conditions, while ERT arrays tracked the moisture movement with a high spatial resolution. The findings support a framework for integrating geophysical methods into risk-based asset management. More studies applying similar approaches are summarized and highlighted in Tables 2–6.

Hybrid systems that combine geophysical methods with data from remote sensing and geotechnical investigations can help reduce the uncertainties of each individual approach. Remote sensing offers broad spatial coverage, fast data collection, and easy integration with GIS, addressing some limitations of the geophysical methods. However, its limited subsurface sensitivity is balanced by geophysics, which provides detailed subsurface imaging at higher resolution, and hence validation opportunities. Moreover, for smaller infrastructure slopes, remote sensing's spatial resolution may be insufficient and may also be impeded by the dense vegetation cover present on some infrastructure slopes [21].

Table 7. Limitations and strengths of each geophysical techniques in landslide monitoring.

Methods	Challenges	Strengths
GPR	Noise contamination [122,202] Signal attenuation and energy loss [122] Signal saturation and false reflections [122] Image and depth distortion [122] Interpretation challenges: [74,193]	Efficient hazard mitigation [195] Post-processing capabilities [202] Soil moisture detection [193] Rapid and cost effective [74] Rapid or real-time time-lapse monitoring Operational flexibility [74] Mobile and cloud integration [74]
Seismic Methods	Cost and time intensity [141]. Traffic noise interference [97]. Access issues in rugged topography [141]. Limited spatial resolution [137]. Sensitivity to seasonal variations detecting [204]. Microseismic signal ambiguity [154]. Complex waveform analysis [49]. Challenges with earthquake locating [49].	Debris flow detection [49] Site effect assessment [49] Landslide slip surface identification [49] Material thickness estimation [49] Remote event monitoring [49] Instantaneous rockfall detection [189] Kinematics of collapse from passive seismic data [137] DAS's continuous coverage and sensitivity to small displacements [44]
Electrical Methods	Non-uniqueness of solution [80] Negative correlation between depth and resolution [80] Data calibration challenges [80] Slower setup and survey design complexity [80] Electrode positioning constraints [80] Software limitations in hydrological analysis [48] Subsoil resistivity issues in water/clay-rich environments [48]. Dependence on main power supply or expensive power alternatives [205] Interference from linear conductive structures (pipelines, power lines) [205] Railway interference due to metallic infrastructure [205] Needs automated data management and processing [205]	Moisture dynamics of unstable slopes with electrical resistivity [137] Illustrating the subsurface heterogeneity [50] High-resolution, time-lapse tomography with active-source techniques in the near surface [137] ERT effectiveness with clear resistivity differences between bedrock and slide material [48] Cost-effective ERT with low-cost electrodes for long-term monitoring [109]. Minimizing topography challenges with resistivity inversion [109]. Process data quickly [50] Capable of obtaining a continuous image of subsurface conditions [50] Ability of covering a vast area in a short amount of time [50]
Electromagnetic methods	Sensitivity to distortions in electromagnetic results [206] Technical expertise required for electromagnetic interpretation [206] Influence of ground characteristics on electromagnetic field propagation [206] Limited positioning precision in geodetic surveys due to air refraction [207]	Single apparent electrical resistivity value for rapid mapping [118] Benefits of frequency domain electromagnetic method (FDEM) for quick surveys [118].

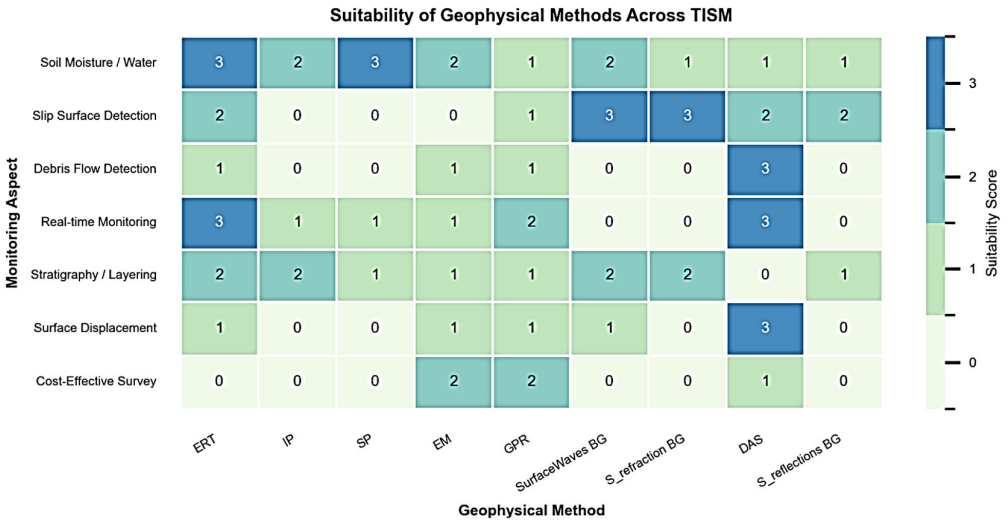

Figure 4. Performance of geophysical methods for key TISM parameters, produced using the same method as in the CIRIA report (ref. [211]).

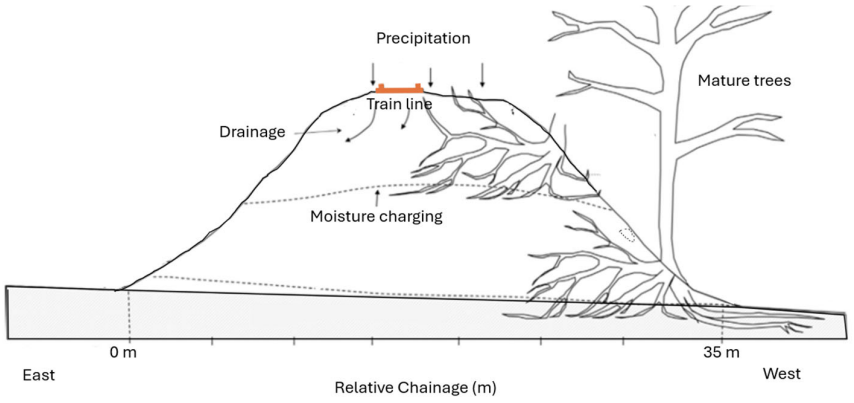

(**a**)

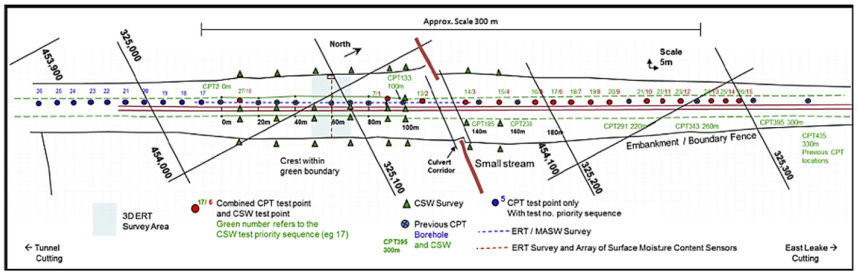

(**b**)

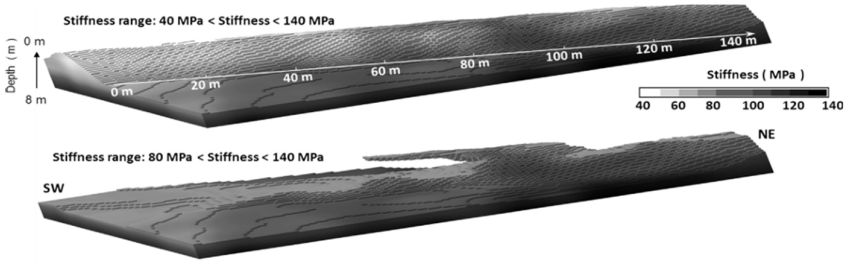

(**c**)

Figure 5. *Cont.*

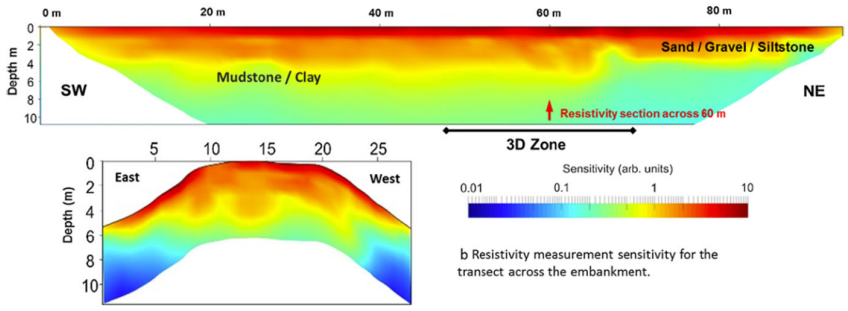

(**d**)

Figure 5. (**a**) Cross-section of the monitored embankment from; (**b**) site investigation layout and sensor deployment; (**c**) 3D subsurface stiffness model derived from surface wave methods (CSW and MASW); (**d**) lateral and vertical sensitivity analysis of resistivity measurements from ERT. Example from a railway infrastructure landslide adapted from ref. [57]. © 2018 Published by Elsevier Ltd.

6. Geophysical–Geotechnical Property Relationships

Besides their assistance in site investigation of costly, structurally complex, and topographically severe slopes, translating geophysical measurement to geotechnical properties is one of the main aspects of using geophysical monitoring in slope stability. Besides natural slope stability by ref. [44], regarding TISM, ref. [43] proved some key advantages of the petrophysical relationship which includes the following: (1) high-resolution imaging of geotechnical processes at scales impractical for traditional sensors; (2) the translation of technical geophysical measurements into properties directly relevant to engineering applications; and (3) the provision of input data for slope-scale physical and process-based models.

Some of the geotechnical parameters significant in tracking slope instability include the moisture content, pore water pressure, hydraulic conductivity, and shear strength which cannot be measured directly through geophysical surveys. These geotechnical parameters, however, can be inferred from geophysical measurements through establishing petrophysical relationships. For example, resistivity measurements have been linked to moisture content ([90,212]) and soil suction ([43]). Moreover, shear strength and pore water pressure have been derived from resistivity measurements in a study conducted by ref. [213].

Seismic methods measure the wave velocity. The wave velocity is sensitive to the rock and soil types and their initial formation pressure, cracks and their pore-filling fluids, kinetic elastic moduli, and material-bearing capacity ([214]). The indirect connections between wave velocity and soil mechanical parameters can be obtained from standard geotechnical tests and used for stability evaluations in geotechnical engineering, according to refs. [215,216]. According to refs. [214,217] kinetic elastic moduli, Poisson's ratio, and the dynamic stiffness of the material, which may be described as dynamic shear and Young's modulus, are crucial mechanical parameters for identifying soil layers and are closely correlated with seismic velocities.

These petrophysical relationships can then be used to calibrate field-scale geophysical models in terms of geotechnical properties. Ultimately, this approach makes time-lapse geophysical imaging a powerful tool for modelling changes in geotechnical properties over time and space (i.e., in four dimensions) at the slope scale. By using petrophysical relationships, it allows us to understand how water moves within the subsurface of slopes [44,213].

- Electrical Methods and Hydraulic Properties

Subsurface hydraulic properties like moisture content, pore water pressure, and hydraulic conductivity can be derived from electrical resistivity methods in landslide monitoring. Ref. [14] applied four-dimensional resistivity measurements to monitor a highway slope in British Columbia, correlating resistivity changes with moisture fluctuations and identifying zones of hydraulic stress before failure. Similarly, ref. [51] utilized resistivity measurements on slopes adjacent to highways, demonstrating their capability to detect moisture redistribution, a precursor to slope instability. Ref. [9] highlighted the importance of time-lapse resistivity data in characterizing the water infiltration pathways in railway embankments, enhancing early warning systems.

- Seismic Methods and Mechanical Properties

Mechanical properties such as shear modulus, stiffness, and the location of deformation zones can be inferred from seismic geophysical techniques. Ref. [57] employed passive seismic monitoring on railway slopes, correlating seismic velocity changes with reductions in shear strength during saturation events. Ref. [197] reviewed the seismic methods for slope monitoring, emphasizing their utility in detecting stress concentrations and areas of potential failure in transportation corridors. Ref. [85] combined seismic surveys with drilling to assess the landslide susceptibility in railway-adjacent slopes, linking seismic velocity anomalies with mechanical weakness.

- Integrated Geophysical Methods

Combining electrical and seismic methods provides comprehensive insights into both hydraulic and mechanical slope characteristics, crucial for maintaining transportation infrastructure. Ref. [218] employed integrated methods to monitor railway slopes in Canada, using ERT and seismic data to model the slope hydrodynamics and mechanical behavior. Ref. [219] presented examples of employing ERT and GPR to identify and monitor the structural weaknesses in embankments, contributing to enhanced transportation safety. Similarly, ref. [220] highlighted the use of integrated ERT and GPR for the maintenance and monitoring of TISs, underscoring their effectiveness in detecting concealed instabilities.

The integration of geophysical techniques—such as geoelectrical and seismic methods—offers a more comprehensive characterization of the subsurface slope conditions, as each method contributes complementary information. This integrative approach is particularly valuable when both mechanical and hydromechanical properties are required for analysis, as highlighted by ref. [221]. In addition to the use of multiple geophysical techniques, enhancing model interpretation and reducing source-specific bias can be achieved by integrating diverse data inputs into a single model. These inputs may include geotechnical data (e.g., inclinometer readings, soil suction, and moisture content), environmental observations (e.g., rainfall records), and remote sensing outputs (e.g., InSAR, LiDAR).

7. Time-Lapse Data Analysis and Forward and Inversion Modelling

According to ref. [11], the term "monitoring" refers to a time-lapse method for examining the differences between two or more geophysical data sets collected at the same site on various dates. The condition of one (or more) properties in the system at a given time is revealed via time-static geophysical data sets, but not how those properties will change in response to an external stimulus (such as precipitation).

The underlying assumption is that a process—such as infiltration—must occur between the two survey times to cause a change in subsurface properties. By analyzing the differences between the datasets collected at the beginning and end of the time period, it is possible to draw reasonable conclusions about the processes that likely occurred within the system. Geoelectrical and seismic monitoring are the two primary techniques used to track

landslides, according to recent research. Although lithological composition often stays fairly stable over time, particularly in a pre-failure situation, moisture dynamics can change significantly. The correlations between moisture content and resistivity demonstrate that time-lapse geoelectrical techniques can be used to infer the hydrological status of a hillslope and, consequently, shear strength and liquid limits, important factors in assessing the slope stability [11]. The loss of stiffness that directly contributes to the failure in the bulk of the material can be measured at depth using the time-lapse seismic approach. As such, it is a supplement to the often-observed signs of surface displacement or rainwater infiltration. Furthermore, ambient noise correlation offers consistent and reliable monitoring even in the presence of precipitation, snow, vegetation, or a line-of-sight problem between the sensors, as indicated in studies by ref. [167,222]. Variations in shear wave velocity reflect changes in the soil's stiffness and density. It is encouraging since failure is directly linked to a loss in stiffness, or softening, in the subsurface strata, which is most likely represented by the decline in seismic velocity [223].

Time-lapse geophysical monitoring provides a dynamic approach to understanding the changes in slope stability over time, offering insights that static or snapshot data alone cannot achieve. Time-lapse monitoring is a powerful tool for TISM, offering a deeper understanding of the processes that influence the slope stability and enhancing early warning systems. The most commonly used and successful geophysical method regarding time lapse TISM includes ERT and DAS [83]; however, UAV-based geophysical sensors [224] have also been successfully applied for real-time TISM.

There are occasions when "time-lapse" or "4D" data sets are used to refer to geophysical techniques that incorporate the addition of a time series to the acquired data. Time lapse will be used in this review to refer to data sets of any dimension (1D, 2D, and 3D) that include multiple time steps because the term, 4D, explicitly refers to a 3D data set with multiple time steps.

8. Challenges and Future Directions

8.1. Monitoring Instrumentation

To provide early warnings and swift action in landslides, real-time monitoring is crucial for early detection and rapid failure warnings [225]. Techniques like ERT, GPR [226], and FOC have advanced beyond the traditional monitoring methods, which exclusively provided snapshots. The PRIME system from British Geological Survey is an example of this progress, using time-lapse ERT to automatically deliver near-real-time data from remote areas [109], capabilities which were unavailable around two decades ago. Similarly, other traditional geophysical methods including seismic methods could be enhanced to provide continuous, real-time soil measurements during TISM with future developments.

8.2. Coupled Modelling/Surveys

Geophysical methods are subject to a variety of uncertainties, which can be mitigated through the use of complementary geotechnical approaches. As highlighted by ref. [49], most of the drawbacks associated with geophysical methods can align with the strengths of geotechnical techniques, and vice versa. This underscores the synergies and complementary nature of these two investigative approaches. Therefore, a particularly effective monitoring approach involves translating geophysical into geotechnical models using petrophysical relationships [118]. The creation of sophisticated coupled hydro-geomechanical models that take geophysical data into account need to be the main goal of future research. These models can shed some light on the relationship between shifting pore pressure and groundwater conditions and slope stability.

Geophysical-geotechnical modelling often faces limitations related to image resolution, cost, and survey scale. These challenges can be addressed by integrating geophysical-geotechnical modelling with real-time data collection technologies, such as UAVs, particularly for large-scale, hard-to-access infrastructure slopes [50]. Despite its potential, the integration of UAVs and geophysical methods in TISM remains underexplored. For example, ref. [50] combined Electrical Resistivity Imaging (ERI) with UAV imaging to monitor four highway embankments, resulting in an optimized technique for monitoring vulnerable TISM.

8.3. Machine Learning/Artificial Intelligence

With the combination of cutting-edge techniques like time-lapse monitoring and artificial intelligence (AI), interpreting and visualizing geophysical data, especially ERT, has received a great deal of attention (e.g., ref. [227]). One notable application of AI in geophysics is to improve time-lapse visualization imaging and estimate high-resolution petrophysical properties which enables the dynamic tracking and analysis of subsurface changes over time [228]. The majority of the automation in time lapse systems is built on machine learning (ML) [229]. Time-lapse imaging algorithms allow for the dynamic visualization and long-term monitoring of subsurface conditions, offering unique insights into temporal fluctuations (e.g., ref. [230]). A time-clustering algorithm is introduced by ref. [230] to enhance the interpretation of time-lapse ERT (TL-ERT) data after inversion, aiming to reliably identify structural facies and hydrofacies. Their work highlighted the value of ML in improving the robustness of ERT-inverted interpretations and distinguishing the subsurface zonation. Other geophysical methods have also been integrated with ML to improve the prediction accuracy of landslides. In a study conducted by ref. [231], the application of ML resulted in an 86% improvement in the prediction accuracy compared to the conventional inverse velocity method traditionally used for slope monitoring. The integration of machine learning with seismic methods for assessing landslide susceptibility further reinforces the potential of ML to enhance data interpretation and improve the reliability of geohazard analysis [232].

ML also can be used to improve the accuracy and precision of landslide susceptibility models, as traditional models and statistical learning approaches may have limitations (e.g., ref. [233]). Moreover, with the use of ML in landslide studies, ref. [234] was able to generate ground models quickly and objectively by grouping geophysical data into cluster groups with comparable measurement ranges and trends. In instances where choices must be made quickly and there may not be enough expertise, ref. [234] used machine learning (ML) to automate the process and minimize the need for human interpretation. As a result, the combination of geophysical methods, time-lapse imaging, and machine learning has the potential to change the way that we think about and use subsurface properties as technology evolves.

8.4. Distributed Acoustic Sensing (DAS)

A fundamental FOC system comprises a light source, optical fiber, sensing components, detectors, and a signal-processing algorithm. Depending on the specific technique employed, FOC systems can measure a wide range of physical parameters, including displacement, strain, stress, vibration, acceleration, temperature, angular velocity, voltage, current, and concentration levels. DAS operates by analyzing the effects of seismic vibrations on light transmission through FOC. The sensitivity of fiber optics to vibrations, coupled with a fast response and a high signal-to-noise ratio, addresses some of the major limitations faced by traditional seismic sensors such as geophones and microtremors [62]. DAS, considered a potential replacement for borehole seismic sensors, is a relatively recent

method of seismic data acquisition that is rapidly gaining traction. According to studies by [235–238], advancements in DAS and related fiber-optic sensing technologies provide an affordable and highly repeatable option for time-lapse vertical seismic profile acquisition. This reduces the reliance on costly wireline geophone deployments, positioning DAS as a popular and emerging substitute for traditional geophones (e.g., refs. [134,239,240]).

DAS offers a range of additional advantages, including superior spatial resolution, flexibility for deployment across diverse environments, continuous seismic data collection over extended distances [190,239–242], and resilience against extreme weather conditions [239]. In the context of landslide monitoring, DAS serves as a real-time monitoring tool, unlike traditional seismic methods, which often offer only a static snapshot of subsurface data. Although there are challenges in accurately localizing seismic sources, DAS presents a more cost-effective approach compared to traditional seismic monitoring techniques for landslides (e.g., refs. [134,239,240]). However, specific research on TISM using DAS remains limited. Recent years have seen growing interest in DAS for TISM applications, with successful studies conducted by ref. [54,134,189,191] highlighting its potential. Given its numerous advantages over the traditional methods, DAS is poised as a highly reliable and promising technology for TISM, meriting further attention and exploration.

8.5. Nodal Seismic Systems

The term "nodal system" is frequently used to describe any seismic acquisition system that uses a cable-less recording unit. This method employs seismic sensor nodes equipped with wireless transceivers to form a network of geophones that communicate via radio frequency technology. When compared to conventional seismic data acquisition, nodal systems offer superior subsurface image quality, flexibility, and automation in surveys [243], as well as the ability to overcome cable constraints [244]. Because of their adaptability, effectiveness, and capacity to provide high-quality seismic data for resource exploration and geological interpretation, according to ref. [244], nodal seismic systems have generally grown in popularity within the seismic exploration sector.

A study conducted by ref. [245] emphasizes the quality of the seismic waveforms collected via nodal seismic systems. They carried out a dense array experiment along the Hayward fault in California, utilizing 182 nodal sensors to obtain high-resolution images of the fault using ambient noise surface-wave tomography. Nodal sensors recorded both local and teleseismic earthquakes with a strong signal-to-noise ratio, as validated by [245]. They discovered that Love and Rayleigh waves could be separated, which would be helpful for imaging subterranean formations.

Ref. [246] conducted a study using nodal geophones to compare their receiver functions to those of conventional seismic stations. According to the findings of their investigation, nodal arrays with a bigger footprint can capture deeper features more precisely than broadband deployments. Ref. [246] state that nodal geophones may offer additional benefits over conventional broadband-only deployments, such as shortened deployment times and lower costs, contingent on the research goal. Nodal geophones are becoming more widely available to independent researchers, and the successful demonstration of nodal geophones as a viable tool for receiver function investigations opens a wide range of scientific subjects for further less expensive investigations.

8.6. Drone-Based Geophysical Sensors

Traditional geophysical sensor methods for wide-area monitoring are often time consuming, unsuitable for real-time monitoring and capturing field-scale variability, and hazardous to access, especially on transportation slopes. These limitations have led researchers to explore innovative approaches, such as integrating drones with geophysical

sensors (e.g., refs. [247,248]). Despite challenges such as limited flight time, load capacity, and communication limitation in urban zones, drones provide a low-cost solution for collecting high-spatial-and-temporal-resolution data across large landscapes. They are simple to deploy and operate, even in hazardous or difficult-to-reach areas, making them suitable for slope monitoring in transportation infrastructure projects [50]. Drone data can be processed using structure-from-motion photogrammetry to generate detailed orthophotos and digital surface models, critical for analyzing slope dynamics and identifying potential hazards [45]. Unmanned Aerial Vehicles (UAVs) can be programmed for real-time site monitoring, ensuring continuous data collection [50]. This capability helps address the limitations of traditional geophysical methods that lack real-time data acquisition, such as seismic, electromagnetic (EM), and ground-penetrating radar (GPR) techniques.

Drones equipped with geophysical sensors efficiently monitor passive and active ground movement, which is crucial for slope stability analysis. Emerging Drones' applications include electromagnetic (e.g., refs. [248,249]), magnetometry (e.g., refs. [250,251]), GPR (e.g., ref. [252]), and large-scale seismic surveys, e.g., ref. [224], sensors for the temporal and spatial monitoring of slopes.

These technologies support the creation of 3D ground and digital terrain models [253], essential for analyzing the slope behaviour near transportation infrastructure. Drone-mounted geophysical sensors are becoming increasingly popular for slope monitoring due to their efficiency, accessibility, and ability to provide high-quality real-time data. These features make them ideal for monitoring and managing the stability of slopes adjacent to transportation infrastructure, thereby reducing risks and ensuring safety.

9. Conclusions

Geophysical methods have been widely used to monitor slopes along railways, roads, and canals. Among these, techniques such as ERT and MASW, together with emerging technologies like FOC, are among the most commonly applied tools. Monitoring designs have included both temporary and permanent setups, with temporary monitoring being more frequent. However, there is increasing interest in real-time and permanent monitoring installations, particularly in applications involving EI and FOC.

These methods reveal the critical subsurface properties and structures, including soil moisture dynamics, landslide slip surfaces, material thickness, subsurface heterogeneity, and the real-time detection of rockfalls and debris flows. For example, seismic techniques are effective for identifying slip surfaces and monitoring dynamic events, while electrical resistivity methods excel in imaging moisture distribution and subsurface variations. Time-lapse monitoring through methods like ERT, DAS, and microtremors offers valuable insights into the slope stability changes over time, enhancing the understanding of slope processes and improving early warning systems.

Each geophysical method brings specific benefits and challenges. GPR is fast and cost effective but struggles with noise and interpretation issues. Seismic techniques provide critical data on slope dynamics but face challenges with cost and spatial resolution. Electrical resistivity methods deliver detailed imaging but can be limited by power constraints and interference. EM techniques are effective for rapid surveys but require expertise and are sensitive to ground conditions. To address these limitations, a multi-method approach combining these techniques is essential for comprehensive and reliable monitoring. Figure 4 demonstrates a summary of the geophysical methods' performance in TISM.

Emerging technologies are transforming TISM. Real-time monitoring systems and advancements in time-lapse inversion have greatly increased the application of geoelectrical methods in this field. Innovations such as DAS, nodal seismic systems, UAV-mounted sensors, and coupled geophysical-geotechnical models enhance accessibility, resolution,

and data validation. The integration of artificial intelligence and machine learning further refines data interpretation, automates processes, and improves predictive modelling.

Transportation infrastructure slopes present unique technical, operational, and safety challenges distinct from natural or general slope settings. These slopes require unique monitoring solutions due to their proximity to critical transport routes and the potential for severe socioeconomic consequences if failure occurs. By highlighting how geophysical methods are specifically adapted for use in Transportation Infrastructure Slope Monitoring (TISM) contexts—both in terms of instrumentation and interpretation—this review fills an important gap in the existing literature.

Future research should focus on applying multiple geophysical techniques, developing integrated frameworks that combine high-resolution geophysical data with real-time monitoring, and leveraging emerging technologies and AI to create safer, more efficient, and cost-effective monitoring solutions. This holistic approach aims to minimize the infrastructure risks, enhance public safety, and optimize the management of transportation slopes.

Author Contributions: Z.R.M.: compilation of references; writing—original draft, revised draft, review, and editing. P.W.: writing—revised draft, review, and editing. J.C.: writing—revised draft, review, and editing. S.D.: writing—revised draft, review, and editing. J.L.H.: writing—revised draft, review, and editing. R.S.: writing—revised draft, review, and editing. All authors have read and agreed to the published version of the manuscript.

Funding: This work was supported by the Natural Environment Research Council (grant number NE/S007431/1) and by the British Geological Survey University Funding Initiative (BUFI) and Network Rail (BGS contract ref. GA/22S/007). The contribution of Donohue was financially supported by Research Ireland, the Geological Survey of Ireland, and the Environmental Protection Agency under the SFI/Research Ireland Frontiers for the Future Programme grant 19/FFP/6535.

Informed Consent Statement: This is a review of the existing literature and does not involve any studies in human or animals' participants. As such, no ethical approval or consent to participate was needed. The authors confirm that they have followed ethical standards in research and publication, including proper citation and acknowledgment of all referenced works.

Data Availability Statement: No new data were created or analyzed in this study. Data sharing is not applicable to this article.

Acknowledgments: This work is published with the permission of the Executive Director at the British Geological Survey.

Conflicts of Interest: The authors declare no conflict of interest.

Appendix A

Table A1. Case Studies on Monitoring TISs Using Near-Surface Geophysical Methods. Note: "-" = not specified; "×" = multiplication.

(**a**) Railway Infrastructure Slopes Monitored via Geophysical Methods				
Reference	**Method/ Survey Design**	**Monitoring Type**	**Grid Geometry**	**Monitoring Period (Days)**
[134]	FOC (DAS)	Temp	3D	-
	FOC array: in shallow trenches (30 cm deep), fully armoured sensing cable. DAS parameters: 1 m channel spacing, 10 m gauge length, 1000 Hz rate. Seismic sources: strikes on a 40 mm thick plate at seven different distances from the midpoint of trenches. Additional sensors: eight three-component nodal seismic stations deployed near the FOC array for reference, sampled synchronously with the DAS unit.			

Table A1. *Cont.*

[56,57]	ERT MASW CSW	ERT (Perm) MASW (temp) CSW (temp)	2D	270
	ERT: Two electrode lines, one parallel to the embankment containing 96 electrodes spaced at 1.5 m. Another line, with 32 electrodes spaced at 1 m, ran over the embankment. A dipole–dipole configuration. CSW: Seismic source: a controlled frequency vertical oscillator containing up to six geophones (4 Hz) conducted across the crest of the embankment and just below the toe of the flanks. Wavelengths ranged from 0.3 m to 15 m, depending on the spacing of geophones. The CSW method generated frequencies from 5 to 200 Hz. The horizontal sampling between CSW locations was 10 m. MASW: Coverage along 140 m by moving successive geophone arrays along the embankment. Seismic source: an impulsive sledgehammer and long geophone arrays (between 24 and 36 geophones). Frequencies generated were limited to below 80 Hz but still allowed the characterization of the shallow subsurface. Geophones were spaced at either 0.5 m or 1 m, covering distances of up to 35 m.			
[56]	CSW MASW	-	2D	-
	CSW: Five profiles of CSW, each containing 13 geophones with 1 and 2 m intervals, measuring signal frequencies up to 200 Hz. CSW surveys were undertaken along a 140 m section of the embankment, at the same stations with MASW and were laid out to complement the MASW survey line. Seven profiles, five of them parallel to the embankment crest; two crossed the embankment. MASW: Three profiles of MASW each containing 13 geophones with 1 m spacing intervals. Signal measuring was limited to frequencies below 100 Hz. MASW surveys were undertaken along a 140 m section of an embankment. Static arrays, with geophone spacing of 1 m.			
[56]	CSW MASW	Temp	2D	120
	MASW: Signal measuring limited to frequencies below 100 Hz. Source: 24-channel land streamer (4.5-Hz), geophones 1 m apart. A 300 m survey line divided into 50 increments, each covering 6 m. Rayleigh wave generator: a hammer/plate source, 2 m away from the nearest geophone. CSW: Measuring signal frequencies up to 200 Hz.			
[55]	MASW CSW	Temp	2D	-
	MASW: Source: 14 lb hammer and plate. Survey along 130 m embankment axis, with a series of static arrays with a 1 m geophone spacing. A total of 24–36 channel arrays of vertically polarized geophones that were spaced either at 0.5 m (array length up to 17.5 m) or 1 m (array lengths to 35 m). Also, a land streamer 24-channel arrays of vertically polarized geophones. CSW: A 130 m survey along the embankment axis; 13 geophones. CSW survey stations were planned with respect to the MASW survey line. Signal frequencies up to 200 Hz were measurable with the CSW, whereas the MASW was often limited to frequencies below 100 Hz.			
[55]	ERT	Temp	2D	540
	A profile (140 m) of 64 electrodes; electrode spacing of 1.5 m; parallel to the embankment transect. Several 32-electrode line arrays across the embankment; electrode spacing of 1 m. Dipole–dipole electrode configuration.			
[55]	ERT	Perm	3D	780
	Twelve cross-axis ERT lines, profile spacing of 2 m; electrode spacing of 1 m. Additional 32-electrode line arrays along the embankment; electrode spacing of 1 m. dipole–dipole array configuration.			
[61]	FOC (DSS)	Perm	2D	420
	Type: Long-gauge fibre Bragg grating (GBG) strain sensors. Sensors: two types: one chain of three borehole sensors (at depths of 38, 40, and 68 m; extending up to 20 m), and two surface extensometers (measure both strain and temperature). Data collection in two modes: (a) dynamic measurements (triggered by deformation) at high sampling rates (100 Hz). (b) Static data logging every 5 min.			

Table A1. *Cont.*

[83]	FOC (DAS)	-	2D	45 days
	Instrument: Febus A1 interrogator; a 10 km dark fibre parallel to the road and rail line (perpendicular to the slope); a gauge length of 8 m; a channel spacing of 4 m; a sampling frequency of 200 Hz.			
[14]	ERT	Semiperm	3D	720 (2 years)
	Two electrode profiles. One ERT line (91 m) with 45 electrodes. The other ERT line (54 m) with 27 electrodes; electrode configuration of Wenner.			
[85]	EM, ERT	ERT (Semiperm) EM(Temp)	2D	120
	ERT: Three longitudinal ERT profiles and three transverse ERT profiles were gathered. Each profile contained 32 electrodes and was 126 m long; electrode spacing of 2 m. Elec. config. of Schlumberger. EM: In the landslide area, three TEM survey lines with respective lengths of 126, 200, and 300 m were set up. The emission frequency was 25 Hz, and the emission current was 1 A. The transmitter coil utilized had a side length of 2 m. A 10 m spot distance was used for measuring spots with the TEM.			
[86]	ERT	Perm	2D and 3D	300 (2D ERT), and 540 (3D ERT)
	Within a 22 m portion of the embankment, a permanent ERT monitoring array was erected, consisting of twelve wires that ran perpendicular to the rails and were spaced 2 m apart. There were 32 electrodes on each line, spaced 1 m apart.			
[87]	ERT	Perm	4D	720
	Two sensor arrays made up the installation: one was 91 m long and had 45 evenly spaced underground rod electrodes, while the other was 54 m long and had 27 evenly spaced buried rod electrodes.			
[43]	ERT	Perm	4D	720
	Buried stainless steel rod electrodes were laid out in five lines, two of which ran uphill and three of which ran downhill, spanning a relict landslide and parts of un-slipped cutting on either side. Lines 1 and 2 had 91 electrodes spaced one m apart, whereas Lines 3, 4, and 5 had 19 electrodes.			
[81]	ERT	Perm	2D	120
	Wenner configuration. Two intersecting ERT profiles: one 91 m with 45 evenly spaced electrodes, the other covered 54 m containing 27 electrodes.			
[59]	EM GPR ERT SR	2D (ERT)	-	30 (EM & GPR) 360 (ERT)
	EM: Two surveys on different days. Two sets of equipment were used: Geonics EM-31 and EM-34 systems operating in a vertical dipole. The EM-31 survey was conducted in a continuous acquisition mode by walking for each survey profile, while the EM-34 data were recorded at stationary points along the survey lines. Real-time global positioning information was integrated with the collected data to accurately georeference the conductivity measurements. GPR: Two surveys: Survey 1. A nominal source frequency of 100 MHz and 50 MHz antennae was used. The antennae were dragged over the slope with a fixed transmitter–receiver separation of 1 m. Continuous data collection was performed at a rate of approximately 15 soundings per second, allowing for detailed mapping of the subsurface. Survey 2. A nominal source frequency of 30 MHz. The survey involved ten lines while travelling downstream in a raft. ERT: One ERT line, Wenner array of 47 ground electrodes spaced every 5 m. Four ERT lines. A reverse Wenner array was used with a minimum electrode separation of 10 m. SRa: Energy source: a Betsy gun and a sledgehammer and steel plate. Three to five shots were taken at each location. Five transect lines. Two Geometrics Geodes and 24–48 geophones, with a spacing of 5 m between the geophones.			

Table A1. *Cont.*

[88]	ERT	Semi-permanent	2D	720
	The resistivity test chambers had interior dimensions of 78 mm × 25 mm × 25 mm, pin electrode separations of 25 mm and 75 mm, and were placed into the specimens at a depth of 5 mm. In accordance with the Wenner approach, a four-point drying curve was generated.			
[87]	ERT	Perm	3D	720
	Five ERT lines, two ERT lines across a slope, 91 electrodes, elec. spacing of 1 m, and three ERT profiles along the slope, 19 elecs., elec. spacing of 1 m. Measurement sets were acquired automatically once every 12 h using a dipole–dipole array configuration.			
[89]	ERT	Perm	2D	over 90
	Five ERT profiles, two parallel to the rail track and three across to the tracks, a Schlumberger array configuration with an inter-electrode spacing of 5 m. No info about the number of electrodes in each profile, and nothing about electrodes or profile spacing.			
[127]	Vp refraction	-	1D (plus time)	180
	The recording array used in all nine acquisition operations was set up with 24, 4.5 Hz, spike linked, and vertical geophones spaced 2 m apart along a straight line on the embankment's crest. A 4.5 kg sledgehammer striking a metal plate was the cause of the seismic event. Along the seismic line, the source was positioned at 16 distinct points. To obtain seismic sections with a higher signal-to-noise ratio, three recordings were taken for each of these source points and then stacked in the time domain.			
[128]	MASW	-	2D	480
	The MASW data were collected utilizing a land streamer made up of 24 vertical geophones with 4.5 Hz along the embankment crest. The geophones were mounted to the ground using cleated metal plates and spaced at 1 m intervals. A 4.5 kg sledgehammer striking a metal plate two m away from the first receiver served as the seismic source. In most cases, a total acquisition time of under 2 h was achieved.			
[90]	ERT	PERM	4D	720
	Ten ERT profiles 3 M apart, each line 24 electrodes, 0.75 M spaced			
[90]	ERT	PERM	4D	720
	One ERT line, 256 electrodes, 1.3 M spaced			

(**b**) Road Infrastructure Slopes Monitored via Geophysical Methods

Reference	Method/ Survey Design	Monitoring Type	Grid Geometry	Monitoring Period (Days)
[91]	ERT	Perm	2D	300
	Two 64-electrode arrays, 0.5 m spacing, dipole–dipole config., AGI Super Sting R8/IP instrument.			
[55]	ERT	Perm	2D	900
	ALERT system, 64 electrodes, 0.5 m spacing across 32 m, dipole–dipole config.			
[129]	AN	Temp	1D	-
	Triaxial accelerometers on ground/slope points, 2–8 m apart, frequency range 0.2–10 Hz.			
[82]	ERT HVSR MAM	- - -	2D 1D 1D	300
	Five profiles: 710 m/470 m/141 m, electrode spacing 3–10 m. HVSR with three-comp. geophones, MAM with 24 synchronized sensors.			
[130]	Microtremor (HVSR)	-	1D	60
	Sixteen locations in the sliding zone; DATAMARK JU410, 15 min records, 100 Hz sampling.			

Table A1. *Cont.*

[61]	FOC Strain	Perm	1D	420
	Sensors: one chain of three borehole sensors, and two surface extensometers. Dynamic measurements (triggered by deformation) at high sampling rates (100 Hz). Static data logging every 5 min.			
[83]	DAS	-	2D	45
	A 10 km dark fibre; a gauge length of 8 m; a channel spacing of 4 m; a sampling frequency of 200 Hz.			
[92]	ERT	Temp	2D	420
	ERT profile containing 96 electrodes, 0.5 m spacing, dipole–dipole configuration.			
[55]	ERT	Perm	2D	900
	Dipole–dipole config. ERT profile made of 64 electrodes, 0.5 m apart, covering 32 m.			
[93]	ERT AN	PERM	ER (2D), S (1D)	365
	ERT: A total of 48 electrodes; 5 m intervals. A dipole–dipole config. AN: A permanent seismological array, continuously recording microseismic events since 2010 at the station. This setup included six vertical velocity sensors placed 50 m from a central three-component 4.5 Hz velocimeter, with all sensors buried at a depth of 1 m and connected to a receiver. The ambient seismic sources included rockfalls and internal quakes.			
[131]	MASW, HVSR	Temp	2D	1589
	MASW: active: two active MASW surveys: December 2010 and April 2015, an array of 12 vertical geophones (4.5 Hz) 4 m and 5 m apart. The energy source of a weight drop was used, and multiple energizations were performed about 8 m from the geophone starter to enhance the signal's energy content relative to the ambient noise. AN: three-component microtremor, 16 min recording duration, 128 Hz sampling frequency. Five HVSR sections were acquired using four compact tomographs (1 dm^3, 1 kg, 2200 V/(m/s) sensitivity, 24 dB, 0.1250 Hz resolution). Environmental noise was recorded at each station for 16 min to ensure signal stability at 128 Hz sampling frequency.			
[94]	S-ANT	Temp	2D	167
	Noise source: local high-frequency seismic noise from heavy vehicular traffic on the road. Two intersecting profiles with the length of 75 and 95. 12 seismometers spaced 10 to 20 m apart,. Record duration: 60 min. Sampling rate: 10 ms. Frequency range: 0.03 to 100 Hz.			
[94]	ERT	Perm	4D	239
	A 224 m ERT profile with varying electrode spacing (1 m at the center, increasing toward the edges).			
[132]	FOC AN	Perm	FOC (2D) AN (1D)	212
	DSS: A strain rosette, embedded 1 m below the surface in the landslide's central part, included three 5 m FOC sensors arranged radially to monitor multi-directional strain changes. Each sensor captured length variations along three directions, enabling 2D strain assessment. AN: Six Geospace GS-11D 4.5 Hz three-component geophones monitored the seismic activity across the GMM. Unique seismic events included the following: Short, high-frequency bursts (up to 100 Hz); longer, lower-frequency events (<60 Hz); low-amplitude, narrowband, lasting 10–30 s; long (>60 s), low frequency (<50 Hz); high-frequency spikes on one station with corresponding low-frequency signals on others. A nearby reference station and sound sensors aided in distinguishing mass movement-induced seismic events from other sources.			

Table A1. *Cont.*

[53]	SR S-CC	-	1D	146
	Two active seismic profiles were performed along and across the landslide. The longitudinal profile used eight geophones at 5 m spacing with explosive shots, while the transverse profile used eight geophones at 8 m spacing with hammer strikes on a plate. Two 2 Hz three-component seismic sensors were buried at 40 cm depth, 35 m apart in stable terrain outside the landslide. Each sensor was connected to a 24-bit Kephren acquisition station, digitizing and storing data at 250 Hz.			
[95]	SPT	Controlled test	2D	1
	(Eleven electrodes separated by 5 m) 50 m profile. The 24 h monitoring phase was a part of the longer semi-permanent monitoring campaign.			
[96]	ERT	-	2D	-
	A 32-electrode system, electrode spacing of 10 to 30 m; a dipole–dipole array arrangement. During the field survey, eight ERT lines with lengths varying from 310 to 600 m were undertaken. Seven lines were oriented transversely to the landslide body; one line was oriented parallel to the accumulation zone. A total of 323 measurements were recorded for each profile.			
[97]	ERT	-	3D (time lapse)	600
	Two linear arrays with 64 electrodes each, each ostensibly located 2 m apart, making up the PRIME system. A dipole–dipole array configuration was used.			
[98]	ERT	Temp	2D	-
	Two ERT profiles; the Wenner-Schlumberger array and the pole–pole array were the two types of electrode arrays used in this study. The "Super-Sting R8" multi-electrode resistivity system was used.			
[60]	ERT, MASW	Temp	2D	342
	ERT: A dipole–dipole arrangement was used. There were 64 electrodes, with 6 m spacing. MASW: A roll-along shear wave velocity imaging across the electrical profiles was performed using 24 geophones (4.5 Hz) spaced 2 m apart with an offset spacing of 4 m. The seismic source was a 10 kg hammer on a metal plate as a cut-off frequency, and the spectral analysis's dramatic amplitude fall around 110 Hz was chosen.			
[50]	ERT	TEMP	2D	over multiple observational periods
	Multiple lines of 2D ERI surveys focusing on post-failure forensic evaluations, with a dipole–dipole array with 56 electrodes spaced at different centre-to-centre distances.			

(**c**) Canal Infrastructure Slopes Monitored via Geophysical Methods

Reference	Method/ Survey Design	Monitoring Type	Grid Geometry	Monitoring Period (Days)
[56]	CSW MASW	-	CSW (2D) MASW (3D)	-
	CSW: Measuring signal frequencies up to 200 Hz. CSW surveys were undertaken along a 140 m section of the embankment, at the same stations with MASW and were laid out to complement the MASW survey line. Seven profiles, five of them parallel to the embankment crest; two crossed the embankment. MASW: Signal measuring limited to frequencies below 100 Hz. Four profiles, each parallel to the canal line and each 17.5 m long; 36 vertical geophones with a series of overlapping 8-channel geophones, spaced at 0.5 m; MASW surveys were undertaken along a 140 m section of an embankment. Static arrays, with geophone spacing of 1 m.			

Table A1. *Cont.*

	S-EDCL	Semipermanent	2D	10
[133]	One three-component sensor was surrounded by six one-component sensors in each of the two deployed tripartite sensor arrays. The seismic arrays used in passive seismic acquisition systems had a radius of 20 and 40 m. A tripartite-shaped array had one three-component (3C) sensor in the centre and six vertical sensors spaced roughly 20 and 40 m apart in each of the three directions. The upper portion of the landslide had two seismic arrays constructed. As the optimal trade-off between signal resolution, data storage, and data transmission, the data sampling rate was set at 400 Hz. For both locations, the ground motion was concurrently recorded on all the channels of each array with a flat frequency response in the frequency range [2–80] Hz.			

References

1. Wang, L.Q.; Xue, X.L.; Zhao, Z.B.; Wang, Z.Y. The Impacts of Transportation Infrastructure on Sustainable Development: Emerging Trends and Challenges. *Int. J. Environ. Res. Public Health* **2018**, *15*, 1172. [CrossRef] [PubMed]
2. Jaiswal, P.; van Westen, C.J. Use of quantitative landslide hazard and risk information for local disaster risk reduction along a transportation corridor: A case study from Nilgiri district, India. *Nat. Hazards* **2013**, *65*, 887–913. [CrossRef]
3. Miele, P.; Di Napoli, M.; Guerriero, L.; Ramondini, M.; Sellers, C.; Corona, M.A.; Di Martire, D. Landslide Awareness System (LAwS) to Increase the Resilience and Safety of Transport Infrastructure: The Case Study of Pan-American Highway (Cuenca-Ecuador). *Remote Sens.* **2021**, *13*, 1564. [CrossRef]
4. Logan, K.G.; Nelson, J.D.; Mclellan, B.C.; Hastings, A. Japan and the UK: Emission predictions of electric and hydrogen trains to 2050. *Transp. Res. Interdisc. Perspect.* **2021**, *10*, 100344. [CrossRef]
5. Jaroszweski, D.; Hooper, E.; Baker, C.; Chapman, L.; Quinn, A. The impacts of the 28 June 2012 storms on UK road and rail transport. *Meteorol. Appl.* **2015**, *22*, 470–476. [CrossRef]
6. Rail, N. Check Before You Travel as Storm Ciara Damage Means Some Journeys Are Disrupted. Available online: https://www.networkrailmediacentre.co.uk/news/check-before-you-travel-as-storm-ciara-damage-means-some-journeys-are-disrupted (accessed on 4 April 2025).
7. Domingues, J.V.M. Natural Hazard Management in Railway Infrastructures Considering a Climate Change Scenario: The North Line: Alfarelos-Pampilhosa Section. Master's Thesis, University of Coimbra, Coimbra, Portugal, 2021.
8. Mair, R. *Earthworks Review: Final Report*; Geotechnical Consulting Group: London, UK, 2021.
9. Smethurst, J.A.; Smith, A.; Uhlemann, S.; Wooff, C.; Chambers, J.; Hughes, P.; Lenart, S.; Saroglou, H.; Springman, S.M.; Löfroth, H.; et al. Current and future role of instrumentation and monitoring in the performance of transport infrastructure slopes. *Q. J. Eng. Geol. Hydrogeol.* **2017**, *50*, 271–286. [CrossRef]
10. Dixon, N.; Smith, A.; Flint, J.A.; Khanna, R.; Clark, B.; Andjelkovic, M. An acoustic emission landslide early warning system for communities in low-income and middle-income countries. *Landslides* **2018**, *15*, 1631–1644. [CrossRef]
11. Whiteley, J.S.; Chambers, J.E.; Uhlemann, S.; Wilkinson, P.B.; Kendall, J.M. Geophysical Monitoring of Moisture-Induced Landslides: A Review. *Rev. Geophys.* **2019**, *57*, 106–145. [CrossRef]
12. Mantovani, F.; Soeters, R.; VanWesten, C.J. Remote sensing techniques for landslide studies and hazard zonation in Europe. *Geomorphology* **1996**, *15*, 213–225. [CrossRef]
13. Kumar, P.; Debele, S.E.; Sahani, J.; Rawat, N.; Marti-Cardona, B.; Alfieri, S.M.; Basu, B.; Basu, A.S.; Bowyer, P.; Charizopoulos, N.; et al. An overview of monitoring methods for assessing the performance of nature-based solutions against natural hazards. *Earth-Sci. Rev.* **2021**, *217*, 103603. [CrossRef]
14. Holmes, J.; Chambers, J.; Meldrum, P.; Wilkinson, P.; Boyd, J.; Williamson, P.; Huntley, D.; Sattler, K.; Elwood, D.; Sivakumar, V.; et al. Four-dimensional electrical resistivity tomography for continuous, near-real-time monitoring of a landslide affecting transport infrastructure in British Columbia, Canada. *Near Surf. Geophys.* **2020**, *18*, 337–351. [CrossRef]
15. Casagli, N.; Intrieri, E.; Tofani, V.; Gigli, G.; Raspini, F. Landslide detection, monitoring and prediction with remote-sensing techniques. *Nat. Rev. Earth. Environ.* **2023**, *4*, 51–64. [CrossRef]
16. Auflic, M.J.; Herrera, G.; Mateos, R.M.; Poyiadji, E.; Quental, L.; Severine, B.; Peternel, T.; Podolszki, L.; Calcaterra, S.; Kociu, A.; et al. Landslide monitoring techniques in the Geological Surveys of Europe. *Landslides* **2023**, *20*, 951–965. [CrossRef]
17. Barla, G.; Antolini, F.; Barla, M.; Mensi, E.; Piovano, G. Monitoring of the Beauregard landslide (Aosta Valley, Italy) using advanced and conventional techniques. *Eng. Geol.* **2010**, *116*, 218–235. [CrossRef]

18. Tarchi, D.; Casagli, N.; Fanti, R.; Leva, D.D.; Luzi, G.; Pasuto, A.; Pieraccini, M.; Silvano, S. Landslide monitoring by using ground-based SAR interferometry: An example of application to the Tessina landslide in Italy. *Eng. Geol.* **2003**, *68*, 15–30. [CrossRef]
19. Niethammer, U.; James, M.R.; Rothmund, S.; Travelletti, J.; Joswig, M. UAV-based remote sensing of the Super-Sauze landslide: Evaluation and results. *Eng. Geol.* **2012**, *128*, 2–11. [CrossRef]
20. Mondini, A.C.; Santangelo, M.; Rocchetti, M.; Rossetto, E.; Manconi, A.; Monserrat, O. Sentinel-1 SAR Amplitude Imagery for Rapid Landslide Detection. *Remote Sens.* **2019**, *11*, 760. [CrossRef]
21. Miller, P.; Mills, J.; Barr, S.; Lim, M.; Barber, D.; Parkin, G.; Clarke, B.; Glendinning, S.; Hall, J. Terrestrial laser scanning for assessing the risk of slope instability along transport corridors. *Int. Arch. Photogramm. Remote Sens. Spat. Inf. Sci.* **2008**, *37*, 495–500.
22. Tsutsui, K.; Rokugawa, S.; Nakagawa, H.; Miyazaki, S.; Cheng, C.T.; Shiraishi, T.; Yang, S.D. Detection and volume estimation of large-scale landslides based on elevation-change analysis using DEMs extracted from high-resolution satellite stereo imagery. *IEEE Trans. Geosci. Remote Sens.* **2007**, *45*, 1681–1696. [CrossRef]
23. Xu, H.; Shu, B.; Zhang, Q.; Du, Y.; Zhang, J.; We, T.; Xiong, G.H.; Dai, X.L.; Wang, L. Site selection for landslide GNSS monitoring stations using InSAR and UAV photogrammetry with analytical hierarchy process. *Landslides* **2024**, *21*, 791–805. [CrossRef]
24. Zhou, P.C.; Han, J.W.; Cheng, G.; Zhang, B.C. Learning Compact and Discriminative Stacked Autoencoder for Hyperspectral Image Classification. *IEEE Trans. Geosci. Remote Sens.* **2019**, *57*, 4823–4833. [CrossRef]
25. Cheng, G.; Yang, C.Y.; Yao, X.W.; Guo, L.; Han, J.W. When Deep Learning Meets Metric Learning: Remote Sensing Image Scene Classification via Learning Discriminative CNNs. *IEEE Trans. Geosci. Remote Sens.* **2018**, *56*, 2811–2821. [CrossRef]
26. Ngo, P.T.T.; Panahi, M.; Khosravi, K.; Ghorbanzadeh, O.; Kariminejad, N.; Cerda, A.; Lee, S. Evaluation of deep learning algorithms for national scale landslide susceptibility mapping of Iran. *Geosci. Front.* **2021**, *12*, 505–519. [CrossRef]
27. Tiranti, D.; Rabuffetti, D. Estimation of rainfall thresholds triggering shallow landslides for an operational warning system implementation. *Landslides* **2010**, *7*, 471–481. [CrossRef]
28. Zhuang, J.Q.; Peng, J.B.; Wang, G.H.; Javed, I.; Wang, Y.; Li, W. Distribution and characteristics of landslide in Loess Plateau: A case study in Shaanxi province. *Eng. Geol.* **2018**, *236*, 89–96. [CrossRef]
29. Lee, M.L.; Ng, K.Y.; Huang, Y.F.; Li, W.C. Rainfall-induced landslides in Hulu Kelang area, Malaysia. *Nat. Hazards* **2014**, *70*, 353–375. [CrossRef]
30. Dikshit, A.; Sarkar, R.; Pradhan, B.; Segoni, S.; Alamri, A.M. Rainfall Induced Landslide Studies in Indian Himalayan Region: A Critical Review. *Appl. Sci.* **2020**, *10*, 2466. [CrossRef]
31. Mu, W.P.; Wu, X.; Qian, C.; Wang, K. Triggering mechanism and reactivation probability of loess-mudstone landslides induced by rainfall infiltration: A case study in Qinghai Province, Northwestern China. *Environ. Earth Sci.* **2020**, *79*, 22. [CrossRef]
32. Mondini, A.C.; Guzzetti, F.; Melillo, M. Deep learning forecast of rainfall-induced shallow landslides. *Nat. Commun.* **2023**, *14*, 2466. [CrossRef]
33. Pagano, L.; Picarelli, L.; Rianna, G.; Urciuoli, G. A simple numerical procedure for timely prediction of precipitation-induced landslides in unsaturated pyroclastic soils. *Landslides* **2010**, *7*, 273–289. [CrossRef]
34. Ma, S.Y.; Shao, X.Y.; Xu, C. Physically-based rainfall-induced landslide thresholds for the Tianshui area of Loess Plateau, China by TRIGRS model. *Catena* **2023**, *233*, 107499. [CrossRef]
35. Argyriou, A.V.; Polykretis, C.; Teeuw, R.M.; Papadopoulos, N. Geoinformatic Analysis of Rainfall-Triggered Landslides in Crete (Greece) Based on Spatial Detection and Hazard Mapping. *Sustainability* **2022**, *14*, 3956. [CrossRef]
36. Lau, Y.M.; Wang, K.L.; Wang, Y.H.; Yiu, W.H.; Ooi, G.H.; Tan, P.S.; Wu, J.; Leung, M.L.; Lui, H.L.; Chen, C.W. Monitoring of rainfall-induced landslides at Songmao and Lushan, Taiwan, using IoT and big data-based monitoring system. *Landslides* **2023**, *20*, 271–296. [CrossRef]
37. Huang, Y.; Zhao, C.Z.; Jin, X.Y.; Zhu, Y.; Peng, M.; Chen, Z.Y. Case study of a landslide continuous probability rainfall threshold analysis based on the prediction interval principle. *Sci. Rep.* **2023**, *13*, 2434. [CrossRef]
38. Baum, R.; Godt, J. Early warning of rainfall-induced shallow landslides and debris flows in the USA. *Landslides* **2010**, *7*, 259–272. [CrossRef]
39. Casadei, M.; Dietrich, W.E. Controls on shallow landslide size. In Proceedings of the 3rd International Conference on Debris-Flow Hazards Mitigation: Mechanics, Prediction, and Assessment, Davos, Swizerland, 10–12 September 2003; Volumes 1 and 2, pp. 91–101.
40. Kaya, A.; Midilli, Ü.M. Slope stability evaluation and monitoring of a landslide: A case study from NE Turkey. *J. Mt. Sci.* **2020**, *17*, 2624–2635. [CrossRef]
41. Imani, P.; Abd El-Raouf, A.; Tian, G. Landslide investigation using Seismic Refraction Tomography method: A review. *Ann. Geophys.* **2021**, *64*, SE657. [CrossRef]
42. Ullah, F.; Su, L.J.; Cheng, L.; Liu, Z.Y.; Hu, B.L. Geophysical prospecting related to earthflow reactivation and hazard assessment: A study based on Huangnibazi slope failure in Sichuan Province, China. *Bull. Eng. Geol. Environ.* **2022**, *81*, 21. [CrossRef]

43. Holmes, J.; Chambers, J.; Wilkinson, P.; Dashwood, B.; Gunn, D.; Cimpoiaşu, M.; Kirkham, M.; Uhlemann, S.; Meldrum, P.; Kuras, O. 4D electrical resistivity tomography for assessing the influence of vegetation and subsurface moisture on railway cutting condition. *Eng. Geol.* **2022**, *307*, 106790. [CrossRef]
44. Whiteley, J.S.; Watlet, A.; Kendall, J.M.; Chambers, J.E. Brief communication: The role of geophysical imaging in local landslide early warning systems. *Nat. Hazards Earth Syst. Sci. Discuss.* **2021**, *21*, 3863–3871. [CrossRef]
45. Hussain, Y.; Schlögel, R.; Innocenti, A.; Hamza, O.; Iannucci, R.; Martino, S.; Havenith, H.B. Review on the Geophysical and UAV-Based Methods Applied to Landslides. *Remote Sens.* **2022**, *14*, 4564. [CrossRef]
46. Lapenna, V.; Perrone, A. Time-Lapse Electrical Resistivity Tomography (TL-ERT) for Landslide Monitoring: Recent Advances and Future Directions. *Appl. Sci.* **2022**, *12*, 1425. [CrossRef]
47. Cho, A.; Joung, I.; Jeong, J.; Song, S.Y.; Nam, M.J. A Review on Past Cases of Geophysical Explorations for Assessment of Slope Stability. *Econ. Environ. Geol.* **2022**, *55*, 111–125. [CrossRef]
48. Perrone, A.; Lapenna, V.; Piscitelli, S. Electrical resistivity tomography technique for landslide investigation: A review. *Earth-Sci. Rev.* **2014**, *135*, 65–82. [CrossRef]
49. Pazzi, V.; Morelli, S.; Fanti, R. A Review of the Advantages and Limitations of Geophysical Investigations in Landslide Studies. *Int. J. Geophys.* **2019**, *2019*, 2983087. [CrossRef]
50. Nobahar, M.; Salunke, R.; Alzeghoul, O.E.; Khan, M.S.; Amini, F. Mapping of Slope Failures on Highway Embankments using Electrical Resistivity Imaging (ERI), Unmanned Aerial Vehicle (UAV), and Finite Element Method (FEM) Numerical Modeling for Forensic Analysis. *Transp. Geotech.* **2023**, *40*, 100949. [CrossRef]
51. Whiteley, J.; Inauen, C.; Wilkinson, P.; Meldrum, P.; Swift, R.; Kuras, O.; Chambers, J. Assessing the risk of slope failure to highway infrastructure using automated time-lapse electrical resistivity tomography monitoring. *Transp. Geotech.* **2023**, *43*, 101129. [CrossRef]
52. Bordoni, M.; Vivaldi, V.; Bonì, R.; Spanò, S.; Tararbra, M.; Lanteri, L.; Parnigoni, M.; Grossi, A.; Figini, S.; Meisina, C. A methodology for the analysis of continuous time-series of automatic inclinometers for slow-moving landslides monitoring in Piemonte region, northern Italy. *Nat. Hazards* **2023**, *115*, 1115–1142. [CrossRef]
53. Mainsant, G.; Larose, E.; Brönnimann, C.; Jongmans, D.; Michoud, C.; Jaboyedoff, M. Ambient seismic noise monitoring of a clay landslide: Toward failure prediction. *J. Geophys. Res. Earth Surf.* **2012**, *117*, F01030. [CrossRef]
54. Trafford, M.S.; Chambers, J.; Dashwood, B.; Crickmore, R.; Harms, J.; Donohue, S. Seasonal Variation in Railway Embankment Condition from Passive Analysis of Train Generated Surface Waves Using DAS. In Proceedings of the NSG 2024 30th European Meeting of Environmental and Engineering Geophysics, Helsinki, Finland, 8–12 September 2024; pp. 1–5.
55. Gunn, D.A.; Chambers, J.E.; Uhlemann, S.; Wilkinson, P.B.; Meldrum, P.I.; Dijkstra, T.A.; Haslam, E.; Kirkham, M.; Wragg, J.; Holyoake, S.; et al. Moisture monitoring in clay embankments using electrical resistivity tomography. *Constr. Build. Mater.* **2015**, *92*, 82–94. [CrossRef]
56. Gunn, D.; Dashwood, B.A.J.; Bergamo, P.; Donohue, S. Aged embankment imaging and assessment using surface waves. *Proc. Inst. Civ. Eng.-Forensic Eng.* **2016**, *169*, 149–165. [CrossRef]
57. Gunn, D.A.; Chambers, J.E.; Dashwood, B.E.; Lacinska, A.; Dijkstra, T.; Uhlemann, S.; Swift, R.; Kirkham, M.; Milodowski, A.; Wragg, J.; et al. Deterioration model and condition monitoring of aged railway embankment using non-invasive geophysics. *Constr. Build. Mater.* **2018**, *170*, 668–678. [CrossRef]
58. Borecka, A.; Herzig, G.; Durjasz-Rybacka, M. Ground penetrating radar investigations of landslides: A case study in a landslide in Radziszów. *Stud. Geotech. Mech.* **2015**, *37*, 11–18. [CrossRef]
59. Huntley, D.; Bobrowsky, P.; Hendry, M.; Macciotta, R.; Best, M. Multi-technique Geophysical Investigation of a Very Slow-moving Landslide near Ashcroft, British Columbia, Canada. *J. Environ. Eng. Geoph.* **2019**, *24*, 87–110. [CrossRef]
60. Su, L.J.; Ullah, F.; Ali, S.; Cheng, L.; Rehman, M.U.; Alam, M. Experimental observation and geophysical modeling of the hydrological effects on Pleistocene glaciation deposits susceptible to landslide. *Int. J. Environ. Sci. Technol.* **2023**, *20*, 1699–1712. [CrossRef]
61. Moore, J.R.; Gischig, V.; Button, E.; Loew, S. Rockslide deformation monitoring with fiber optic strain sensors. *Nat. Hazards Earth Syst. Sci.* **2010**, *10*, 191–201. [CrossRef]
62. Xie, Z.Y.; Sun, Y.W.; Lv, A.Q.; Xu, Q. Measurement and Evaluation Method of Distributed Optical Fiber Acoustic Sensing Performance. *Photonics* **2024**, *11*, 166. [CrossRef]
63. Chen, Y.L.; Wu, P.; Yu, Q.; Xu, G. Effects of Freezing and Thawing Cycle on Mechanical Properties and Stability of Soft Rock Slope. *Adv. Mater. Sci. Eng.* **2017**, *2017*, 3173659. [CrossRef]
64. Zhao, Y.X.; Wang, L.Q.; Li, H. Effect of Freeze-Thaw on the Stability of a Cutting Slope in a High-Latitude and Low-Altitude Permafrost Region. *Appl. Syst. Innov.* **2020**, *3*, 36. [CrossRef]
65. Hua, W.; Dong, S.M.; Li, Y.F.; Xu, J.G.; Wang, Q.Y. The influence of cyclic wetting and drying on the fracture toughness of sandstone. *Int. J. Rock. Mech. Min.* **2015**, *78*, 331–335. [CrossRef]

66. Li, G.Y.; Wang, F.; Ma, W.; Fortier, R.; Mu, Y.H.; Mao, Y.C.; Hou, X. Variations in strength and deformation of compacted loess exposed to wetting-drying and freeze-thaw cycles. *Cold Reg. Sci. Technol.* **2018**, *151*, 159–167. [CrossRef]
67. Mukhlisin, M.; Khiyon, K.N. The Effects of Cracking on Slope Stability. *J. Geol. Soc. India* **2018**, *91*, 704–710. [CrossRef]
68. Lu, Y.; Chen, X.; Wang, L. Research on fracture mechanism and stability of slope with tensile cracks. *Appl. Sci.* **2022**, *12*, 12687. [CrossRef]
69. Emadi-Tafti, M.; Ataie-Ashtiani, B.; Hosseini, S.M. Integrated impacts of vegetation and soil type on slope stability: A case study of Kheyrud Forest, Iran. *Ecol. Model.* **2021**, *446*, 109498. [CrossRef]
70. Singeisen, C.S. Initiation and Mechanisms of Rock Slope Failures During the 2016 Mw 7.8 Kaikōura Earthquake, New Zealand. Ph.D. Thesis, University of Canterbury, Christchurch, New Zealand, 2023.
71. Kolapo, P.; Oniyide, G.O.; Said, K.O.; Lawal, A.I.; Onifade, M.; Munemo, P. An Overview of Slope Failure in Mining Operations. *Mining* **2022**, *2*, 350–384. [CrossRef]
72. Samouëlian, A.; Cousin, I.; Tabbagh, A.; Bruand, A.; Richard, G. Electrical resistivity survey in soil science: A review. *Soil Tillage Res.* **2005**, *83*, 173–193. [CrossRef]
73. Tang, C.S.; Wang, D.Y.; Zhu, C.; Zhou, Q.Y.; Xu, S.K.; Shi, B. Characterizing drying-induced clayey soil desiccation cracking process using electrical resistivity method. *Appl. Clay Sci.* **2018**, *152*, 101–112. [CrossRef]
74. Rasol, M.; Pais, J.C.; Pérez-Gracia, V.; Solla, M.; Fernandes, F.M.; Fontul, S.; Ayala-Cabrera, D.; Schmidt, F.; Assadollahi, H. GPR monitoring for road transport infrastructure: A systematic review and machine learning insights. *Constr. Build. Mater.* **2022**, *324*, 126686. [CrossRef]
75. Uhlemann, S.; Hagedorn, S.; Dashwood, B.; Maurer, H.; Gunn, D.; Dijkstra, T.; Chambers, J. Landslide characterization using P- and S-wave seismic refraction tomography—The importance of elastic moduli. *J. Appl. Geophys.* **2016**, *134*, 64–76. [CrossRef]
76. Romero-Ruiz, A.; Linde, N.; Keller, T.; Or, D. A Review of Geophysical Methods for Soil Structure Characterization. *Rev. Geophys.* **2018**, *56*, 672–697. [CrossRef]
77. Rolia, E.; Sutjiningsih, D. Application of Geoelectric Method for Groundwater Exploration from Surface (A Literature Study). *AIP Conf. Proc.* **2018**, *1977*, 020018. [CrossRef]
78. Deep, M.A.L.; Araffa, S.A.S.; Mansour, S.A.; Taha, A.I.; Mohamed, A.; Othman, A. Geophysics and remote sensing applications for groundwater exploration in fractured basement: A case study from Abha area, Saudi Arabia. *J. Afr. Earth Sci.* **2021**, *184*, 104368. [CrossRef]
79. Loiseau, B.; Carrière, S.D.; Jougnot, D.; Singha, K.; Mary, B.; Delpierre, N.; Guérin, R.; Martin-StPaul, N.K. The geophysical toolbox applied to forest ecosystems-A review. *Sci. Total Environ.* **2023**, *899*, 165503. [CrossRef]
80. Loke, M.H.; Chambers, J.E.; Rucker, D.F.; Kuras, O.; Wilkinson, P.B. Recent developments in the direct-current geoelectrical imaging method. *J. Appl. Geophys.* **2013**, *95*, 135–156. [CrossRef]
81. Huntley, D.; Bobrowsky, P.; Hendry, M.; Macciotta, R.; Elwood, D.; Sattler, K.; Best, M.; Chambers, J.; Meldrum, P. Application of multi-dimensional electrical resistivity tomography datasets to investigate a very slow-moving landslide near Ashcroft, British Columbia, Canada. *Landslides* **2019**, *16*, 1033–1042. [CrossRef]
82. Calamita, G.; Gallipoli, M.R.; Gueguen, E.; Sinisi, R.; Summa, V.; Vignola, L.; Stabile, T.A.; Bellanova, J.; Piscitelli, S.; Perrone, A. Integrated geophysical and geological surveys reveal new details of the large Montescaglioso (southern Italy) landslide of December 2013. *Eng. Geol.* **2023**, *313*, 106984. [CrossRef]
83. Kang, J.H.; Walter, F.; Paitz, P.; Aichele, J.; Edme, P.; Meier, L.; Fichtner, A. Automatic Monitoring of Rock-Slope Failures Using Distributed Acoustic Sensing and Semi-Supervised Learning. *Geophys. Res. Lett.* **2024**, *51*, e2024GL110672. [CrossRef]
84. Marescot, L.; Monnet, R.; Chapellier, D. Resistivity and induced polarization surveys for slope instability studies in the Swiss Alps. *Eng. Geol.* **2008**, *98*, 18–28. [CrossRef]
85. Su, M.X.; Cheng, K.; Liu, Y.M.; Xue, Y.G.; Wang, P.; Zhang, K.; Li, C.C. Combining geophysical methods, drilling, and monitoring techniques to investigate carbonaceous shale landslides along a railway line: A case study on Jiheng Railway, China. *Bull. Eng. Geol. Environ.* **2021**, *80*, 7493–7506. [CrossRef]
86. Chambers, J.E.; Gunn, D.A.; Wilkinson, P.B.; Meldrum, P.I.; Haslam, E.; Holyoake, S.; Kirkham, M.; Kuras, O.; Merritt, A.; Wragg, J. 4D electrical resistivity tomography monitoring of soil moisture dynamics in an operational railway embankment. *Near Surf. Geophys.* **2014**, *12*, 61–72. [CrossRef]
87. Chambers, J.; Holmes, J.; Whiteley, J.; Boyd, J.; Meldrum, P.; Wilkinson, P.; Kuras, O.; Swift, R.; Harrison, H.; Glendinning, S. Long-term geoelectrical monitoring of landslides in natural and engineered slopes. *Lead. Edge* **2022**, *41*, 768–776. [CrossRef]
88. Hen-Jones, R.M.; Hughes, P.N.; Stirling, R.A.; Glendinning, S.; Chambers, J.E.; Gunn, D.A.; Cui, Y.J. Seasonal effects on geophysical-geotechnical relationships and their implications for electrical resistivity tomography monitoring of slopes. *Acta Geotech.* **2017**, *12*, 1159–1173. [CrossRef]
89. Tohari, A.; Koizumi, K.; Syahbana, A.J.; Oda, K. Understanding of Landslide Movement at Bumi Waluya Railway Station, Garut, Indonesia. In *Advancing Culture of Living with Landslides, Volume 2: Advances in Landslide Science*; Springer: Cham, Switzerland, 2017; pp. 319–328. [CrossRef]

90. Maleki, Z.R.; Wilkinson, P.; Swift, R.; Meldrum, P.; Harrison, H.; Camacho, X.K.C.; Ngui, J.; Kuras, O.; Harms, J.; Jessamy, G.; et al. Assessment of railway infrastructure slope failure by automated time-lapse ERT monitoring. In Proceedings of the EGU General Assembly 2024, Vienna, Austria, 14–19 April 2024.
91. Glendinning, S.; Hughes, P.; Helm, P.; Chambers, J.; Mendes, J.; Gunn, D.; Wilkinson, P.; Uhlemann, S. Construction, management and maintenance of embankments used for road and rail infrastructure: Implications of weather induced pore water pressures. *Acta Geotech.* **2014**, *9*, 799–816. [CrossRef]
92. Moradi, S.; Heinze, T.; Budler, J.; Gunatilake, T.; Kemna, A.; Huisman, J.A. Combining Site Characterization, Monitoring and Hydromechanical Modeling for Assessing Slope Stability. *Land* **2021**, *10*, 423. [CrossRef]
93. Palis, E.; Lebourg, T.; Tric, E.; Malet, J.P.; Vidal, M. Long-term monitoring of a large deep-seated landslide (La Clapiere, South-East French Alps): Initial study. *Landslides* **2017**, *14*, 155–170. [CrossRef]
94. Harba, P.; Pilecki, Z. Assessment of time-spatial changes of shear wave velocities of flysch formation prone to mass movements by seismic interferometry with the use of ambient noise. *Landslides* **2017**, *14*, 1225–1233. [CrossRef]
95. Colangelo, G.; Lapenna, V.; Perrone, A.; Piscitelli, S.; Telesca, L. 2D Self-Potential tomographies for studying groundwater flows in the Varco d'Izzo landslide (Basilicata, southern Italy). *Eng. Geol.* **2006**, *88*, 274–286. [CrossRef]
96. Perrone, A.; Iannuzzi, A.; Lapenna, V.; Lorenzo, P.; Piscitelli, S.; Rizzo, E.; Sdao, F. High-resolution electrical imaging of the Varco d'Izzo earthflow (southern Italy). *J. Appl. Geophys.* **2004**, *56*, 17–29. [CrossRef]
97. Montgomery, J.; Kiernan, M.; Jackson, D.; McDonald, B. Integrating Surface-Based Geophysics into Landslide Investigations along Highways. In Proceedings of the Geo-Congress 2022: Geophysical and Earthquake Engineering and Soil Dynamics, Charlotte, NC, USA, 20–23 March 2022; Volume 334, pp. 180–191.
98. Eulilli, V.; Ferri, F.; Puzzilli, L.M. The Role of Geophysics in Urban Landslides Studies: Two Case Histories in Rome. In *Engineering Geology for Society and Territory, Volume 5: Urban Geology, Sustainable Planning and Landscape Exploitation*; Springer: Cham, Switzerland, 2015; pp. 853–856. [CrossRef]
99. Chambers, J.; Goff, C.; Slater, N.; Meldrum, P.; Wilkinson, P.; Gunn, D. Long-term monitoring of sub-surface change in earth embankment dams. In Proceedings of the INCOLD 2021 Symposium, New Delhi, India, 24–27 February 2021.
100. Hu, K.Y.; Huang, Q.H.; Tang, M.G.; Xue, L.; Han, P. Self-potential variations associated with the slip of Huangnibazi Landslide. *J. Appl. Geophys.* **2024**, *220*, 105275. [CrossRef]
101. Tso, C.H.M.; Iglesias, M.; Binley, A. Ensemble Kalman inversion of induced polarization data. *Geophys. J. Int.* **2024**, *236*, 1877–1900. [CrossRef]
102. Revil, A.; Ahmed, A.S.; Coperey, A.; Ravanel, L.; Sharma, R.; Panwar, N. Induced polarization as a tool to characterize shallow landslides. *J. Hydrol.* **2020**, *589*, 125369. [CrossRef]
103. Carrier, A.; Meric, O.; Bottelin, P. Characterizing landslide dynamics from time-lapse time domain induced polarization and ground-based imaging: A case study of the MontGombert landslide (French, Alps). *Landslides* **2024**, *21*, 353–369. [CrossRef]
104. Loke, M.H.; Lane, J.W. Inversion of data from electrical resistivity imaging surveys in water-covered areas. *Explor. Geophys.* **2004**, *35*, 266–271. [CrossRef]
105. Yilmaz, S. Investigation of Gurbulak landslide using 2D electrical resistivity image profiling method (Trabzon, Northeastern Turkey). *J. Environ. Eng. Geoph.* **2007**, *12*, 199–205. [CrossRef]
106. Crawford, M.M.; Bryson, L.S. Assessment of active landslides using field electrical measurements. *Eng. Geol.* **2018**, *233*, 146–159. [CrossRef]
107. Terzaghi, K.; Peck, R.B. *Introduction to Soil Mechanics*; University of Illinois: Urbana, IL, USA, 1943.
108. Zeng, R.Q.; Meng, X.M.; Zhang, F.Y.; Wang, S.Y.; Cui, Z.J.; Zhang, M.S.; Zhang, Y.; Chen, G. Characterizing hydrological processes on loess slopes using electrical resistivity tomography—A case study of the Heifangtai Terrace, Northwest China. *J. Hydrol.* **2016**, *541*, 742–753. [CrossRef]
109. Chambers, J.; Meldrum, P.; Wilkinson, P.; Holmes, J.; Huntley, D.; Bobrowsky, P.T.; Gunn, D.; Uhlemann, S.; Slater, N. Long-Term Geophysical Monitoring of Moisture Driven Landslide Processes. In *Understanding and Reducing Landslide Disaster Risk: Volume 3 Monitoring and Early Warning*; Casagli, N., Tofani, V., Sassa, K., Bobrowsky, P.T., Takara, K., Eds.; Springer International Publishing: Cham, Switzerland, 2021; pp. 67–74. [CrossRef]
110. Slater, L.; Binley, A. Advancing hydrological process understanding from long-term resistivity monitoring systems. *Wiley Interdiscip. Rev. Water* **2021**, *8*, e1513. [CrossRef]
111. Chen, T.T.; Hung, Y.C.; Hsueh, M.W.; Yeh, Y.H.; Weng, K.W. Evaluating the Application of Electrical Resistivity Tomography for Investigating Seawater Intrusion. *Electronics* **2018**, *7*, 107. [CrossRef]
112. Dimech, A.; Cheng, L.Z.; Chouteau, M.; Chambers, J.; Uhlemann, S.; Wilkinson, P.; Meldrum, P.; Mary, B.; Fabien-Ouellet, G.; Isabelle, A. A Review on Applications of Time-Lapse Electrical Resistivity Tomography Over the Last 30 Years: Perspectives for Mining Waste Monitoring. *Surv. Geophys.* **2022**, *43*, 1699–1759. [CrossRef]
113. Loke, M.H.; Wilkinson, P.B.; Chambers, J.E.; Uhlemann, S.; Dijkstra, T.; Dahlin, T. The use of asymmetric time constraints in 4-D ERT inversion. *J. Appl. Geophys.* **2022**, *197*, 104536. [CrossRef]

114. Wilkinson, P.B.; Chambers, J.E.; Meldrum, P.I.; Kuras, O.; Inauen, C.M.; Swift, R.T.; Curioni, G.; Uhlemann, S.; Graham, J.; Atherton, N. Windowed 4D inversion for near real-time geoelectrical monitoring applications. *Front. Earth Sci.* **2022**, *10*, 983603. [CrossRef]
115. Uhlemann, S.; Chambers, J.; Wilkinson, P.; Maurer, H.; Merritt, A.; Meldrum, P.; Kuras, O.; Gunn, D.; Smith, A.; Dijkstra, T. Four-dimensional imaging of moisture dynamics during landslide reactivation. *J. Geophys. Res. Earth Surf.* **2017**, *122*, 398–418. [CrossRef]
116. Uhlemann, S.; Wilkinson, P.B.; Maurer, H.; Wagner, F.M.; Johnson, T.C.; Chambers, J.E. Optimized survey design for electrical resistivity tomography: Combined optimization of measurement configuration and electrode placement. *Geophys. J. Int.* **2018**, *214*, 108–121. [CrossRef]
117. Singha, K.; Day-Lewis, F.D.; Johnson, T.; Slater, L.D. Advances in interpretation of subsurface processes with time-lapse electrical imaging. *Hydrol. Process.* **2015**, *29*, 1549–1576. [CrossRef]
118. Jongmans, D.; Garambois, S. Geophysical investigation of landslides: A review. *Bull. Société Géologique Fr.* **2007**, *178*, 101–112. [CrossRef]
119. Wilkinson, P.B.; Uhlemann, S.; Chambers, J.E.; Meldrum, P.I.; Loke, M.H. Development and testing of displacement inversion to track electrode movements on 3-D electrical resistivity tomography monitoring grids. *Geophys. J. Int.* **2015**, *200*, 1566–1581. [CrossRef]
120. Wilkinson, P.B.; Chambers, J.E.; Meldrum, P.I.; Gunn, D.A.; Ogilvy, R.D.; Kuras, O. Predicting the movements of permanently installed electrodes on an active landslide using time-lapse geoelectrical resistivity data only. *Geophys. J. Int.* **2010**, *183*, 543–556. [CrossRef]
121. Parsekian, A.D.; Singha, K.; Minsley, B.J.; Holbrook, W.S.; Slater, L. Multiscale geophysical imaging of the critical zone. *Rev. Geophys.* **2015**, *53*, 1–26. [CrossRef]
122. Neal, A. Ground-penetrating radar and its use in sedimentology: Principles, problems and progress. *Earth-Sci. Rev.* **2004**, *66*, 261–330. [CrossRef]
123. Tsai, C.C.; Lin, C.H. Review and Future Perspective of Geophysical Methods Applied in Nearshore Site Characterization. *J. Mar. Sci. Eng.* **2022**, *10*, 344. [CrossRef]
124. Miller, R.D.; Steeples, D.W. A Shallow Seismic-Reflection Survey in Basalts of the Snake River Plain, Idaho. *Geophysics* **1990**, *55*, 761–768. [CrossRef]
125. Uyanik, O. Estimation of the porosity of clay soils using seismic P- and S-wave velocities. *J. Appl. Geophys.* **2019**, *170*, 103832. [CrossRef]
126. Kurlenya, M.V.; Serdyukov, A.S.; Chernyshov, G.S.; Yablokov, A.V.; Dergach, P.A.; Duchkov, A.A. Procedure and evidence of seismic research into physical properties of cohesive soils. *J. Min. Sci.* **2016**, *52*, 417–423. [CrossRef]
127. Bergamo, P.; Dashwood, B.; Uhlemann, S.; Swift, R.; Chambers, J.E.; Gunn, D.A.; Donohue, S. Time-lapse monitoring of fluid-induced geophysical property variations within an unstable earthwork using P-wave refraction. *Geophysics* **2016**, *81*, EN17–EN27. [CrossRef]
128. Bergamo, P.; Dashwood, B.; Uhlemann, S.; Swift, R.; Chambers, J.E.; Gunn, D.A.; Donohue, S. Time-lapse monitoring of climate effects on earthworks using surface waves. *Geophysics* **2016**, *81*, EN1–EN15. [CrossRef]
129. Yang, Y.R.; Lee, T.T.; Wang, T.T. Spatiotemporal characteristics of ground microtremor in advance of rockfalls. *Sci. Rep.* **2022**, *12*, 7751. [CrossRef]
130. Liu, P.H.; Wu, J.H.; Lee, D.H.; Lin, Y.H. Detecting landslide vulnerability using anisotropic microtremors and vulnerability index. *Eng. Geol.* **2023**, *323*, 107240. [CrossRef]
131. Imposa, S.; Grassi, S.; Fazio, F.; Rannisi, G.; Cino, P. Geophysical surveys to study a landslide body (north-eastern Sicily). *Nat. Hazards* **2017**, *86*, S327–S343. [CrossRef]
132. Brückl, E.; Brunner, F.K.; Lang, E.; Mertl, S.; Müller, M.; Stary, U. The Gradenbach Observatory-monitoring deep-seated gravitational slope deformation by geodetic, hydrological, and seismological methods. *Landslides* **2013**, *10*, 815–829. [CrossRef]
133. Tonnellier, A.; Helmstetter, A.; Malet, J.P.; Schmittbuhl, J.; Corsini, A.; Joswig, M. Seismic monitoring of soft-rock landslides: The Super-Sauze and Valoria case studies. *Geophys. J. Int.* **2013**, *193*, 1515–1536. [CrossRef]
134. Xie, T.; Zhang, C.C.; Shi, B.; Chen, Z.; Zhang, Y. Integrating distributed acoustic sensing and computer vision for real-time seismic location of landslides and rockfalls along linear infrastructure. *Landslides* **2024**, *21*, 1941–1959. [CrossRef]
135. Ma, Z.N.; Qian, R.Y. Overview of seismic methods for urban underground space. *Interpretation* **2020**, *8*, SU19–SU30. [CrossRef]
136. Akingboye, A.S.; Ogunyele, A.C. Insight into seismic refraction and electrical resistivity tomography techniques in subsurface investigations. *Rud.-Geološko-Naft. Zbornik* **2019**, *34*, 93–111. [CrossRef]
137. Whiteley, J.S.; Chambers, J.E.; Uhlemann, S.; Boyd, J.; Cimpoiasu, M.O.; Holmes, J.L.; Inauen, C.M.; Watlet, A.; Hawley-Sibbett, L.R.; Sujitapan, C.; et al. Landslide monitoring using seismic refraction tomography—The importance of incorporating topographic variations. *Eng. Geol.* **2020**, *268*, 105525. [CrossRef]

138. Heincke, B.; Maurer, H.; Green, A.G.; Willenberg, H.; Spillmann, T.; Burlini, L. Characterizing an unstable mountain slope using shallow 2D and 3D seismic tomography. *Geophysics* **2006**, *71*, B241–B256. [CrossRef]
139. Donohue, S.; Long, M.; O'Connor, P.; Helle, T.E.; Pfaffhuber, A.A.; Romoen, M. Multi-method geophysical mapping of quick clay. *Near Surf. Geophys.* **2012**, *10*, 207–219. [CrossRef]
140. Yamakawa, Y.; Kosugi, K.; Masaoka, N.; Sumida, J.; Tani, M.; Mizuyama, T. Combined geophysical methods for detecting soil thickness distribution on a weathered granitic hillslope. *Geomorphology* **2012**, *145*, 56–69. [CrossRef]
141. Bruno, F.; Martillier, F. Test of high-resolution seismic reflection and other geophysical techniques on the Boup landslide in the Swiss Alps. *Surv. Geophys.* **2000**, *21*, 333–348. [CrossRef]
142. Dehghannejad, M.; Malehmir, A.; Svensson, M.; Lindén, M.; Möller, H. High-resolution reflection seismic imaging for the planning of a double-train-track tunnel in the city of Varberg, southwest Sweden. *Near Surf. Geophys.* **2017**, *15*, 226–240. [CrossRef]
143. Rahimi, S.; Wood, C.M.; Kokkali, P.; Rivers, B. Advantages of Geophysics to Improve Site Characterization and Reliability for Transportation Projects. *Transp. Res. Rec.* **2021**, *2675*, 540–554. [CrossRef]
144. Tomás, R.; Abellán, A.; Cano, M.; Riquelme, A.; Tenza-Abril, A.J.; Baeza-Brotons, F.; Saval, J.M.; Jaboyedoff, M. A multidisciplinary approach for the investigation of a rock spreading on an urban slope. *Landslides* **2018**, *15*, 199–217. [CrossRef]
145. Zakaria, M.T.; Muztaza, N.M.; Zabidi, H.; Salleh, A.N.; Mahmud, N.; Rosli, F.N. Integrated analysis of geophysical approaches for slope failure characterisation. *Environ. Earth Sci.* **2022**, *81*, 299. [CrossRef]
146. Meng, F.S.; Zhang, G.; Qi, Y.P.; Zhou, Y.D.; Zhao, X.Q.; Ge, K.B. Application of combined electrical resistivity tomography and seismic reflection method to explore hidden active faults in Pingwu, Sichuan, China. *Open Geosci.* **2020**, *12*, 174–189. [CrossRef]
147. Malehmir, A.; Saleem, M.U.; Bastani, M. High-resolution reflection seismic investigations of quick-clay and associated formations at a landslide scar in southwest Sweden. *J. Appl. Geophys.* **2013**, *92*, 84–102. [CrossRef]
148. Pertuz, T.; Malehmir, A. Ultrahigh-resolution shear-wave reflection imaging of vertical-component data in a quick-clay prone to landslide area in southwest Sweden. *Geophysics* **2023**, *88*, B121–B133. [CrossRef]
149. Petronio, L.; Boaga, J.; Cassiani, G. Characterization of the Vajont landslide (North-Eastern Italy) by means of reflection and surface wave seismics. *J. Appl. Geophys.* **2016**, *128*, 58–67. [CrossRef]
150. Shan, C.L.; Bastani, M.; Malehmir, A.; Persson, L.; Lundberg, E. Integration of controlled-source and radio magnetotellurics, electric resistivity tomography, and reflection seismics to delineate 3D structures of a quick-clay landslide site in southwest of Sweden. *Geophysics* **2016**, *81*, B13–B29. [CrossRef]
151. Marciniak, A.; Kowalczyk, S.; Gontar, T.; Owoc, B.; Nawrot, A.; Luks, B.; Cader, J.; Majdanski, M. Integrated geophysical imaging of a mountain landslide—A case study from the Outer Carpathians, Poland. *J. Appl. Geophys.* **2021**, *191*, 104364. [CrossRef]
152. Park, C.B.; Miller, R.D.; Xia, J. Multichannel analysis of surface waves. *Geophysics* **1999**, *64*, 800–808. [CrossRef]
153. Donohue, S.; Long, M. Assessment of an MASW technique incorporating discrete. *J. Environ. Eng. Geophys.* **2008**, *13*, 57–68. [CrossRef]
154. Hussain, Y.; Martinez-Carvajal, H.; Cárdenas-Soto, M.; Martino, S. Introductory review of potential applications of nanoseismic monitoring in seismic energy characterization. *J. Eng. Res.* **2019**, *7*, 89–104.
155. Iannucci, R.; Martino, S.; Paciello, A.; D'Amico, S.; Galea, P. Engineering geological zonation of a complex landslide system through seismic ambient noise measurements at the Selmun Promontory (Malta). *Geophys. J. Int.* **2018**, *213*, 1146–1161. [CrossRef]
156. Cankurtaranlar, A.; Demirbag, E. Utilization of ambient noise seismic interferometry to retrieve P-wave reflections at Soma coal basin, Western Turkey. *Geophys. Prospect.* **2023**, *71*, 1356–1367. [CrossRef]
157. Lei, X.Q.; Zhang, J.; Jin, W.Y.; Han, C.; Xu, X.W. The application of ambient noise and reflection seismic exploration in an urban active fault survey. *Interpretation* **2020**, *8*, SU1–SU10. [CrossRef]
158. Wapenaar, K.; Slob, E.; Snieder, R. On seismic interferometry, the generalized optical theorem, and the scattering matrix of a point scatterer. *Geophysics* **2010**, *75*, SA27–SA35. [CrossRef]
159. Harba, P.; Pilecki, Z.; Krawiec, K. Comparison of MASW and seismic interferometry with use of ambient noise for estimation of S-wave velocity field in landslide subsurface. *Acta Geophys.* **2019**, *67*, 1875–1883. [CrossRef]
160. Bensen, G.D.; Ritzwoller, M.H.; Barmin, M.P.; Levshin, A.L.; Lin, F.; Moschetti, M.P.; Shapiro, N.M.; Yang, Y. Processing seismic ambient noise data to obtain reliable broad-band surface wave dispersion measurements. *Geophys. J. Int.* **2007**, *169*, 1239–1260. [CrossRef]
161. Stork, A.L.; Allmark, C.; Curtis, A.; Kendall, J.M.; White, D.J. Assessing the potential to use repeated ambient noise seismic tomography to detect CO leaks: Application to the Aquistore storage site. *Int. J. Greenh. Gas Control* **2018**, *71*, 20–35. [CrossRef]
162. Renalier, F.; Bièvre, G.; Jongmans, D.; Campillo, M.; Bard, P.Y. Clayey Landslide Investigations Using Active and Passive Measurements. In *Advances in Near-Surface Seismology and Ground-Penetrating Radar*; Society of Exploration Geophysicists, American Geophysical Union, Environmental and Engineering Geophysical Society: Houston, TX, USA, 2010; Volume 15, pp. 397–413. [CrossRef]
163. Bontemps, N.; Lacroix, P.; Larose, E.; Jara, J.; Taipe, E. Rain and small earthquakes maintain a slow-moving landslide in a persistent critical state. *Nat. Commun.* **2020**, *11*, 780. [CrossRef]

164. Colombero, C.; Baillet, L.; Comina, C.; Jongmans, D.; Larose, E.; Valentin, J.; Vinciguerra, S. Integration of ambient seismic noise monitoring, displacement and meteorological measurements to infer the temperature-controlled long-term evolution of a complex prone-to-fall cliff. *Geophys. J. Int.* **2018**, *213*, 1876–1897. [CrossRef]
165. Fiolleau, S.; Jongmans, D.; Bièvre, G.; Chambon, G.; Baillet, L.; Vial, B. Seismic characterization of a clay-block rupture in Harmaliere landslide, French Western Alps. *Geophys. J. Int.* **2020**, *221*, 1777–1788. [CrossRef]
166. Renalier, F.; Jongmans, D.; Campillo, M.; Bard, P.Y. Shear wave velocity imaging of the Avignonet landslide (France) using ambient noise cross correlation. *J. Geophys. Res. Earth Surf.* **2010**, *115*, F03032. [CrossRef]
167. Le Breton, M.; Bontemps, N.; Guillemot, A.; Baillet, L.; Larose, É. Landslide monitoring using seismic ambient noise correlation: Challenges and applications. *Earth-Sci. Rev.* **2021**, *216*, 103518. [CrossRef]
168. Del Gaudio, V.; Luo, Y.H.; Wang, Y.S.; Wasowski, J. Using ambient noise to characterise seismic slope response: The case of Qiaozhuang peri-urban hillslopes (Sichuan, China). *Eng. Geol.* **2018**, *246*, 374–390. [CrossRef]
169. Chatelain, J.L.; Guillier, B.; Cara, F.; Duval, A.M.; Atakan, K.; Bard, P.Y.; Team, W.S. Evaluation of the influence of experimental conditions on H/V results from ambient noise recordings. *Bull. Earthq. Eng.* **2008**, *6*, 33–74. [CrossRef]
170. Kleinbrod, U.; Burjánek, J.; Fäh, D. Ambient vibration classification of unstable rock slopes: A systematic approach. *Eng. Geol.* **2019**, *249*, 198–217. [CrossRef]
171. Song, C.; Yu, C.; Li, Z.H.; Pazzi, V.; Del Soldato, M.; Cruz, A.; Utili, S. Landslide geometry and activity in Villa de la Independencia (Bolivia) revealed by InSAR and seismic noise measurements. *Landslides* **2021**, *18*, 2721–2737. [CrossRef]
172. Guo, Z.; Zhou, M.; Huang, Y.; Pu, J.; Zhou, S.; Fu, B.Y.; Aydin, A. Monitoring performance of slopes via ambient seismic noise recordings: Case study in a colluvium deposit. *Eng. Geol.* **2023**, *324*, 107268. [CrossRef]
173. Bozzano, F.; Lenti, L.; Martino, S.; Montagna, A.; Paciello, A. Earthquake triggering of landslides in highly jointed rock masses: Reconstruction of the 1783 Scilla rock avalanche (Italy). *Geomorphology* **2011**, *129*, 294–308. [CrossRef]
174. Bozzano, F.; Lenti, L.; Martino, S.; Paciello, A.; Mugnozza, G.S. Self-excitation process due to local seismic amplification responsible for the reactivation of the Salcito landslide (Italy) on 31 October 2002. *J. Geophys. Res. Solid Earth* **2008**, *113*, B10312. [CrossRef]
175. Danneels, G.; Bourdeau, C.; Torgoev, I.; Havenith, H.B. Geophysical investigation and dynamic modelling of unstable slopes: Case-study of Kainama (Kyrgyzstan). *Geophys. J. Int.* **2008**, *175*, 17–34. [CrossRef]
176. Keskinsezer, A.; Dag, E. Investigating of soil features and landslide risk in Western-Atakent (Istanbul) using resistivity, MASW, Microtremor and boreholes methods. *Open Geosci.* **2019**, *11*, 1112–1128. [CrossRef]
177. Abdelrahman, K.; Al-Otaibi, N.; Ibrahim, E.; Binsadoon, A. Landslide susceptibility assessment and their disastrous impact on Makkah Al-Mukarramah urban Expansion, Saudi Arabia, using microtremor measurements. *J. King Saud Univ. Sci.* **2021**, *33*, 101450. [CrossRef]
178. Partsinevelos, P.; Kritikakis, G.; Economou, N.; Agioutantis, Z.; Tripolitsiotis, A.; Mertikas, S.; Vafidis, A. Integration of seismic and image data processing for rockfall monitoring and early warning along transportation networks. *Nat. Hazards* **2016**, *83*, S133–S153. [CrossRef]
179. Rebert, T.; Cai, C.F.; Hallier, A.; Bardainne, T. Rockfall alarm system for railway monitoring: Integrating seismic detection, localization, and characterization. *Geophysics* **2024**, *89*, KS13–KS23. [CrossRef]
180. Manconi, A.; Coviello, V.; Galletti, M.; Seifert, R. Short Communication: Monitoring rockfalls with the Raspberry Shake. *Earth Surf. Dyn.* **2018**, *6*, 1219–1227. [CrossRef]
181. Bottelin, P.; Baillet, L.; Larose, E.; Jongmans, D.; Hantz, D.; Brenguier, O.; Cadet, H.; Helmstetter, A. Monitoring rock reinforcement works with ambient vibrations: La Bourne case study (Vercors, France). *Eng. Geol.* **2017**, *226*, 136–145. [CrossRef]
182. Vouillamoz, N.; Rothmund, S.; Joswig, M. Characterizing the complexity of microseismic signals at slow-moving clay-rich debris slides: The Super-Sauze (southeastern France) and Pechgraben (Upper Austria) case studies. *Earth Surf. Dyn.* **2018**, *6*, 525–550. [CrossRef]
183. Got, J.L.; Mourot, P.; Grangeon, J. Pre-failure behaviour of an unstable limestone cliff from displacement and seismic data. *Nat. Hazards Earth Syst. Sci.* **2010**, *10*, 819–829. [CrossRef]
184. Gomberg, J.; Schulz, W.; Bodin, P.; Kean, J. Seismic and geodetic signatures of fault slip at the Slumgullion Landslide Natural Laboratory. *J. Geophys. Res. Solid Earth* **2011**, *116*, B09404. [CrossRef]
185. Walter, M.; Walser, M.; Joswig, M. Mapping Rainfall-Triggered Slidequakes and Seismic Landslide-Volume Estimation at Heumoes Slope. *Vadose Zone J.* **2011**, *10*, 487–495. [CrossRef]
186. Provost, F.; Hibert, C.; Malet, J.P. Automatic classification of endogenous landslide seismicity using the Random Forest supervised classifier. *Geophys. Res. Lett.* **2017**, *44*, 113–120. [CrossRef]
187. Yfantis, G.; Pytharouli, S.; Lunn, R.J.; Carvajal, H.E.M. Microseismic monitoring illuminates phases of slope failure in soft soils. *Eng. Geol.* **2021**, *280*, 105940. [CrossRef]

188. Zhang, T.W.; Zhang, X.L.; Ke, X.; Liu, C.; Xu, X.W.; Zhan, X.; Wang, C.; Ahmad, I.; Zhou, Y.; Pan, D.C.; et al. HOG-ShipCLSNet: A Novel Deep Learning Network With HOG Feature Fusion for SAR Ship Classification. *IEEE Trans. Geosci. Remote Sens.* **2022**, *60*, 5210322. [CrossRef]
189. Ravet, F.; Briffod, F.; Goy, A.; Rochat, E. Mitigation of geohazard risk along transportation infrastructures with optical fiber distributed sensing. *J. Civ. Struct. Health Monit.* **2021**, *11*, 967–988. [CrossRef]
190. Hartog, A.H. *An Introduction to Distributed Optical Fibre Sensors*; Series in Fiber Optic Sensors; CRC Press; Taylor & Francis Group: Boca Raton, FL, USA, 2017; 440p.
191. Thevenet, E.; Toubiana, H.; Trafford, A.; Donohue, S.; Harms, J.; Bardainne, T. Assessing 3D Slope Condition with Fibre Optic Seismic Imaging Using Trains as Sources. In Proceedings of the NSG 2024 30th European Meeting of Environmental and Engineering Geophysics, Helsinki, Finland, 8–12 September 2024; pp. 1–5.
192. Wu, K.; Rodriguez, G.A.; Zajc, M.; Jacquemin, E.; Clément, M.; De Coster, A.; Lambot, S. A new drone-borne GPR for soil moisture mapping. *Remote Sens. Environ.* **2019**, *235*, 111456. [CrossRef]
193. Klotzsche, A.; Lärm, L.; Vanderborght, J.; Cai, G.C.; Morandage, S.; Zörner, M.; Vereecken, H.; van der Kruk, J. Monitoring Soil Water Content Using Time-Lapse Horizontal Borehole GPR Data at the Field-Plot Scale. *Vadose Zone J.* **2019**, *18*, 190044. [CrossRef]
194. Caldeira, B.; Oliveira, R.J.; Teixidó, T.; Borges, J.F.; Henriques, R.; Carneiro, A.; Peña, J.A. Studying the Construction of Floor Mosaics in the Roman Villa of Pisoes (Portugal) Using Noninvasive Methods: High-Resolution 3D GPR and Photogrammetry. *Remote Sens.* **2019**, *11*, 1882. [CrossRef]
195. Kannaujiya, S.; Chattoraj, S.L.; Jayalath, D.; Ray, P.K.C.; Bajaj, K.; Podali, S.; Bisht, M.P.S. Integration of satellite remote sensing and geophysical techniques (electrical resistivity tomography and ground penetrating radar) for landslide characterization at Kunjethi (Kalimath), Garhwal Himalaya, India. *Nat. Hazards* **2019**, *97*, 1191–1208. [CrossRef]
196. Lissak, C.; Maquaire, O.; Malet, J.-P.; Lavigne, F.; Virmoux, C.; Gomez, C.; Davidson, R. Ground-penetrating radar observations for estimating the vertical displacement of rotational landslides. *Nat. Hazards Earth Syts.Sci.* **2015**, *15*, 1399–1406. [CrossRef]
197. Mccann, D.M.; Forster, A. Reconnaissance Geophysical Methods in Landslide Investigations. *Eng. Geol.* **1990**, *29*, 59–78. [CrossRef]
198. Boaga, J. The use of FDEM in hydrogeophysics: A review. *J. Appl. Geophys.* **2017**, *139*, 36–46. [CrossRef]
199. Auken, E.; Boesen, T.; Christiansen, A.V. A Review of Airborne Electromagnetic Methods With Focus on Geotechnical and Hydrological Applications From 2007 to 2017. *Adv. Geophys.* **2017**, *58*, 47–93. [CrossRef]
200. Lai, W.W.L.; Dérobert, X.; Annan, P. A review of Ground Penetrating Radar application in civil engineering: A 30-year journey from Locating and Testing to Imaging and Diagnosis. *Ndt&E Int.* **2018**, *96*, 58–78. [CrossRef]
201. Reiss, S.; Reicherter, K.R.; Reuther, C.-D. Visualization and characterization of active normal faults and associated sediments by high-resolution GPR. In *Ground Penetrating Radar in Sediments*; Geological Society, London, Special Publications: London, UK, 2003; Volume 211, pp. 247–255.
202. Anderson, N.L.; Ismael, A.M.; Thitimakorn, T. Ground-penetrating radar: A tool for monitoring bridge scour. *Environ. Eng. Geosci.* **2007**, *13*, 1–10. [CrossRef]
203. Fabregat, I.; Gutiérrez, F.; Roqué, C.; Comas, X.; Zarroca, M.; Carbonel, D.; Guerrero, J.; Linares, R. Reconstructing the internal structure and long-term evolution of hazardous sinkholes combining trenching, electrical resistivity imaging (ERI) and ground penetrating radar (GPR). *Geomorphology* **2017**, *285*, 287–304. [CrossRef]
204. Hussain, Y.; Cardenas-Soto, M.; Martino, S.; Moreira, C.; Borges, W.; Hamza, O.; Prado, R.; Uagoda, R.; Rodríguez-Rebolledo, J.; Silva, R.C.; et al. Multiple Geophysical Techniques for Investigation and Monitoring of Sobradinho Landslide, Brazil. *Sustainability* **2019**, *11*, 6672. [CrossRef]
205. Kiernan, M.; Jackson, D.; Montgomery, J.; Anderson, J.B.; McDonald, B.W.; Davis, K.C. Characterization of a Karst Site using Electrical Resistivity Tomography and Seismic Full Waveform Inversion. *J. Environ. Eng. Geoph.* **2021**, *26*, 1–11. [CrossRef]
206. Pavoni, M.; Sirch, F.; Boaga, J. Electrical and Electromagnetic Geophysical Prospecting for the Monitoring of Rock Glaciers in the Dolomites, Northeast Italy. *Sensors* **2021**, *21*, 1294. [CrossRef]
207. Savvaidis, P. Existing landslide monitoring systems and techniques. In *From Stars to Earth and Culture*; School of Rural and Surveying Engineering, The Aristotle University of Thessaloniki: Thessaloniki, Greece, 2003; pp. 242–258.
208. Sass, O.; Bell, R.; Glade, T. Comparison of GPR, 2D-resistivity and traditional techniques for the subsurface exploration of the Oschingen landslide, Swabian Alb (Germany). *Geomorphology* **2008**, *93*, 89–103. [CrossRef]
209. Bichler, A.; Bobrowsky, P.; Best, M.; Douma, M.; Hunter, J.; Calvert, T.; Burns, R. Three-dimensional mapping of a landslide using a multi-geophysical approach: The Quesnel Forks landslide. *Landslides* **2004**, *1*, 29–40. [CrossRef]
210. Steuer, A.; Smirnova, M.; Becken, M.; Schiffler, M.; Günther, T.; Rochlitz, R.; Yogeshwar, P.; Mörbe, W.; Siemon, B.; Costabel, S.; et al. Comparison of novel semi-airborne electromagnetic data with multi-scale geophysical, petrophysical and geological data from Schleiz, Germany. *J. Appl. Geophys.* **2020**, *182*, 104172. [CrossRef]
211. Usher, C.; Stringfellow, M.; Grossey, T. *Good Practice Guide to Using Geophysics in Ground Investigation*; CIRIA: London, UK, 2023.

212. Merritt, A.J.; Chambers, J.E.; Wilkinson, P.B.; West, L.J.; Murphy, W.; Gunn, D.; Uhlemann, S. Measurement and modelling of moisture-electrical resistivity relationship of fine-grained unsaturated soils and electrical anisotropy. *J. Appl. Geophys.* **2016**, *124*, 155–165. [CrossRef]
213. Boyd, J.P.; Binley, A.; Wilkinson, P.; Holmes, J.; Bruce, E.; Chambers, J. Practical considerations for using petrophysics and geoelectrical methods on clay rich landslides. *Eng. Geol.* **2024**, *334*, 107506. [CrossRef]
214. Othman, A.A.A. Construed geotechnical characteristics of foundation beds by seismic measurements. *J. Geophys. Eng.* **2005**, *2*, 126–138. [CrossRef]
215. Arato, A.; Vagnon, F.; Comina, C. First application of a new seismo-electric streamer for combined resistivity and seismic measurements along linearly extended earth structures. *Near Surf. Geophys.* **2022**, *20*, 117–134. [CrossRef]
216. Kramer, S.L.; Stewart, J.P. *Geotechnical Earthquake Engineering*, 2nd ed.; CRC Press: Boca Raton, FL, USA, 2025.
217. Karl, L.; Fechner, T.; Schevenels, M.; François, S.; Degrande, G. Geotechnical characterization of a river dyke by surface waves. *Near Surf. Geophys.* **2011**, *9*, 515–527. [CrossRef]
218. Huntley, D.; Bobrowsky, P.; MacLeod, R.; Rotheram-Clarke, D.; Cocking, R.; Joseph, J.; Holmes, J.; Sattler, K.; Chambers, J.; Meldrum, P.; et al. IPL Project 202: Landslide Monitoring Best Practices for Climate-Resilient Railway Transportation Corridors in Southwestern British Columbia, Canada. In *Progress in Landslide Research and Technology, Volume 1 Issue 1, 2022*; Sassa, K., Konagai, K., Tiwari, B., Arbanas, Ž., Sassa, S., Eds.; Springer International Publishing: Cham, Switzerland, 2023; pp. 249–265.
219. Malehmir, A.; Socco, L.V.; Bastani, M.; Krawczyk, C.; Pfaffhuber, A.; Miller, R.D.; Maurer, H.; Frauenfelder, R.; Suto, K.; Bazin, S.; et al. Near-Surface Geophysical Characterization of Areas Prone to Natural Hazards: A Review of the Current and Perspective on the Future. *Adv. Geophys.* **2016**, *57*, 51–146.
220. Solla, M.; Pérez-Gracia, V.; Fontul, S. A Review of GPR Application on Transport Infrastructures: Troubleshooting and Best Practices. *Remote Sens.* **2021**, *13*, 672. [CrossRef]
221. Boyd, J. Hydrogeophysical Characterisation for Improved Early Warning of Landslides. Ph.D. Thesis, Lancaster University, Lancaster, UK, 2024.
222. Intrieri, E.; Gigli, G.; Mugnai, F.; Fanti, R.; Casagli, N. Design and implementation of a landslide early warning system. *Eng. Geol.* **2012**, *147*, 124–136. [CrossRef]
223. Hussien, M.N.; Karray, M. Shear wave velocity as a geotechnical parameter: An overview. *Can. Geotech. J.* **2016**, *53*, 252–272. [CrossRef]
224. Hamasato, Y.; Sakaguchi, A.; Tsuji, T.; Yamamoto, K. Optimization of Drone-Based Surface-Wave Seismic Surveys Using a Multiple Traveling Salesman Problem. *J. Robot. Mechatron.* **2023**, *35*, 271–278. [CrossRef]
225. Ramesh, M.; IEEE. Real-time Wireless Sensor Network for Landslide Detection. In Proceedings of the 2009 3rd International Conference on Sensor Technologies and Applications (Sensorcomm 2009), Athens, Greece, 18–23 June 2009; pp. 405–409.
226. Klotzsche, A.; Vereecken, H.; van der Kruk, J. Review of crosshole ground-penetrating radar full-waveform inversion of experimental data: Recent developments, challenges, and pitfalls. *Geophysics* **2019**, *84*, H13–H28. [CrossRef]
227. Hung, Y.C.; Zhao, Y.X.; Hung, W.C. Development of an Underground Tunnels Detection Algorithm for Electrical Resistivity Tomography Based on Deep Learning. *Appl. Sci.* **2022**, *12*, 639. [CrossRef]
228. Pelemo-Daniels, D.; Stewart, R.R. Petrophysical Property Prediction from Seismic Inversion Attributes Using Rock Physics and Machine Learning: Volve Field, North Sea. *Appl. Sci.* **2024**, *14*, 1345. [CrossRef]
229. Yeung, S.; Downing, N.L.; Li, F.F.; Milstein, A. Bedside Computer Vision—Moving Artificial Intelligence from Driver Assistance to Patient Safety. *N. Engl. J. Med.* **2018**, *378*, 1271–1273. [CrossRef]
230. Delforge, D.; Watlet, A.; Kaufmann, O.; Van Camp, M.; Vanclooster, M. Time-series clustering approaches for subsurface zonation and hydrofacies detection using a real time-lapse electrical resistivity dataset. *J. Appl. Geophys.* **2021**, *184*, 104203. [CrossRef]
231. Kothari, U.C.; Momayez, M. Machine learning: A novel approach to predicting slope instabilities. *Int. J. Geophys.* **2018**, *2018*, 4861254. [CrossRef]
232. Dindar, H.; Alevkayalı, Ç. Determination of GIS-based landslide susceptibility and ground dynamics with geophysical measurements and machine learning algorithms. *Int. J. Geosynth. Ground Eng.* **2023**, *9*, 52. [CrossRef]
233. Merghadi, A.; Yunus, A.P.; Dou, J.; Whiteley, J.; ThaiPham, B.; Bui, D.T.; Avtar, R.; Abderrahmane, B. Machine learning methods for landslide susceptibility studies: A comparative overview of algorithm performance. *Earth-Sci. Rev.* **2020**, *207*, 103225. [CrossRef]
234. Whiteley, J.S.; Watlet, A.; Uhlemann, S.; Wilkinson, P.; Boyd, J.P.; Jordan, C.; Kendall, J.M.; Chambers, J.E. Rapid characterisation of landslide heterogeneity using unsupervised classification of electrical resistivity and seismic refraction surveys. *Eng. Geol.* **2021**, *290*, 106189. [CrossRef]
235. Mateeva, A.; Lopez, J.; Potters, H.; Mestayer, J.; Cox, B.; Kiyashchenko, D.; Wills, P.; Grandi, S.; Hornman, K.; Kuvshinov, B.; et al. Distributed acoustic sensing for reservoir monitoring with vertical seismic profiling. *Geophys. Prospect.* **2014**, *62*, 679–692. [CrossRef]
236. Harris, K.; White, D.; Melanson, D.; Samson, C.; Daley, T.M. Feasibility of time-lapse VSP monitoring at the Aquistore CO storage site using a distributed acoustic sensing system. *Int. J. Greenh. Gas Control* **2016**, *50*, 248–260. [CrossRef]

237. Titov, A.; Ji, G.; Binder, G.; Tura, A. Distributed acoustic sensing time-lapse vertical seismic profiling during zipper-fracturing operations: Observations, modeling, and interpretation. *Geophysics* **2022**, *87*, B329–B336. [CrossRef]
238. Zhao, X.M.; Willis, M.E.; Inks, T.; Wilson, G.A. Quantifying hydraulically induced fracture height and density from rapid time-lapse distributed acoustic sensing vertical seismic profile data. *Geophysics* **2021**, *86*, A15–A20. [CrossRef]
239. Mad Zahir, M.H.; Abdul Aziz, K.M.; Ghazali, A.R.; Abdul Latiff, A.H. Effectiveness of Fiber Optic Distributed Acoustic Sensing (DAS) in Vertical Seismic Profiling (VSP) Field Survey. *Appl. Sci.* **2023**, *13*, 5002. [CrossRef]
240. Xie, T.; Zhang, C.C.; Shi, B.; Wang, Z.; Zhang, S.S.; Yin, J. Seismic monitoring of rockfalls using distributed acoustic sensing. *Eng. Geol.* **2023**, *325*, 107285. [CrossRef]
241. Cheng, F.; Chi, B.X.; Lindsey, N.J.; Dawe, T.C.; Ajo-Franklin, J.B. Utilizing distributed acoustic sensing and ocean bottom fiber optic cables for submarine structural characterization. *Sci. Rep.* **2021**, *11*, 5613. [CrossRef]
242. Lindsey, N.J.; Martin, E.R. Fiber-Optic Seismology. *Annu. Rev. Earth Planet. Sci.* **2021**, *49*, 309–336. [CrossRef]
243. Payani, A.; Abdi, A.; Tian, X.; Fekri, F.; Mohandes, M. Advances in Seismic Data Compression via Learning from Data. *IEEE Signal Process. Mag.* **2018**, *35*, 51–61. [CrossRef]
244. Makama, A.; Kuladinithi, K.; Timm-Giel, A. Wireless Geophone Networks for Land Seismic Data Acquisition: A Survey, Tutorial and Performance Evaluation. *Sensors* **2021**, *21*, 5171. [CrossRef]
245. Taira, T.; Dreger, D.S.; Allam, A.A. Nodal Seismic Experiment at the Berkeley Section of the Hayward Fault. *Seismol. Res. Lett.* **2022**, *93*, 2377–2388. [CrossRef]
246. Ward, K.M.; Lin, F.; Schmandt, B. High-Resolution Receiver Function Imaging Across the Cascadia Subduction Zone Using a Dense Nodal Array. *Geophys. Res. Lett.* **2018**, *45*, 12218–12225. [CrossRef]
247. Mitsuhata, Y.; Ueda, T.; Kamimura, A.; Kato, S.; Takeuchi, A.; Aduma, C.; Yokota, T. Development of a drone-borne electromagnetic survey system for searching for buried vehicles and soil resistivity mapping. *Near Surf. Geophys.* **2022**, *20*, 16–29. [CrossRef]
248. Karaoulis, M.; Ritsema, I.; Bremmer, C.; De Kleine, M.; Essink, G.O.; Ahlrichs, E. Drone-Borne Electromagnetic (DR-EM) Surveying in The Netherlands: Lab and Field Validation Results. *Remote Sens.* **2022**, *14*, 5335. [CrossRef]
249. Walter, C.; Braun, A.; Fotopoulos, G. Characterizing electromagnetic interference signals for unmanned aerial vehicle geophysical surveys. *Geophysics* **2021**, *86*, J21–J32. [CrossRef]
250. Porras, D.; Carrasco, J.; Carrasco, P.; Alfageme, S.; Gonzalez-Aguilera, D.; Lopez Guijarro, R. Drone Magnetometry in Mining Research. An Application in the Study of Triassic Cu-Co-Ni Mineralizations in the Estancias Mountain Range, Almeria (Spain). *Drones* **2021**, *5*, 151. [CrossRef]
251. Yoo, L.S.; Lee, J.H.; Lee, Y.K.; Jung, S.K.; Choi, Y. Application of a Drone Magnetometer System to Military Mine Detection in the Demilitarized Zone. *Sensors* **2021**, *21*, 3175. [CrossRef]
252. Vergnano, A.; Franco, D.; Godio, A. Drone-Borne Ground-Penetrating Radar for Snow Cover Mapping. *Remote Sens.* **2022**, *14*, 1763. [CrossRef]
253. Giordan, D.; Adams, M.S.; Aicardi, I.; Alicandro, M.; Allasia, P.; Baldo, M.; De Berardinis, P.; Dominici, D.; Godone, D.; Hobbs, P.; et al. The use of unmanned aerial vehicles (UAVs) for engineering geology applications. *Bull. Eng. Geol. Environ.* **2020**, *79*, 3437–3481. [CrossRef]